Journal of Materials Chemistry C

ROYAL SOCIETY OF CHEMISTRY

REVIEW

View Article Online
View Journal | View Issue

Cite this: J. Mater. Chem. C, 2025, 13, 20806

Aggregation-induced new functions: structure–property relationships in molecular crystals

Yu Zhang, Bing Bai, Gian Albert Alfani, Zheng Zhao * and Ben Zhong Tang *

Molecular crystals, as ordered aggregates of organic molecules, exhibit unique photophysical properties distinct from their monomeric counterparts. Rooted in the emerging framework of aggregate science, this review highlights how collective behaviors (such as arising from intermolecular interactions, symmetry breaking, and crystalline packing) fundamentally reshape excited-state dynamics and energy conversion pathways. We examine recent advances in crystal engineering and cocrystal strategies that enable tunable room-temperature phosphorescence, radical emission, near-infrared luminescence, and efficient photothermal conversion. Through case studies of lone-pair interactions, radical stabilization, and donor–acceptor cocrystals, we elucidate how molecular assemblies can activate new optoelectronic functions inaccessible to isolated molecules. By bridging structure–property relationships from isolated molecules to crystalline states, this review offers a unified perspective on the role of aggregation in functional material design. Looking ahead, aggregate science will continue to guide the discovery of next-generation materials by integrating structural precision, dynamic responsiveness, and multiscale energy manipulation in condensed molecular systems.

Received 30th June 2025,
Accepted 21st July 2025

DOI: 10.1039/d5tc02505b

rsc.li/materials-c

1. Introduction

Molecules have long been defined as the smallest particles of a substance that retain all the properties of the substance.[1] Based on this reductionism paradigm, it was long believed that the properties of molecules determined the behavior of their aggregates.[2] Rooted in reductionism, this research paradigm has been widely adopted in chemistry and materials science, enabling the establishment of structure–property relationships at the molecular level. However, this paradigm does not always hold true. In many systems, the properties of molecular aggregates do not exhibit a linear correlation with those of their constituent monomers. For example, some luminophores show

Guangdong Basic Research Center of Excellence for Aggregate Science, School of Science and Engineering, Shenzhen Institute of Aggregate Science and Technology, The Chinese University of Hong Kong, Shenzhen (CUHK-Shenzhen), Guangdong 518172, P. R. China. E-mail: zhaozheng@cuhk.edu.cn, tangbenz@cuhk.edu.cn

Yu Zhang

Yu Zhang is a PhD candidate (supervisor: Prof. Zheng Zhao) at the School of Science and Engineering, The Chinese University of Hong Kong, Shenzhen, and the Guangdong Basic Research Center of Excellence for Aggregate Science. He received his BS degree in 2023 from the College of Chemistry, Zhengzhou University. His research interests lie in molecular crystal engineering and aggregate-state photophysics, with a particular emphasis on room-temperature phosphorescence (RTP), triplet exciton dynamics, and the development of multifunctional organic luminophores for bioimaging and therapeutic applications.

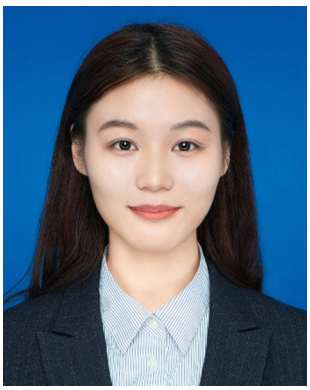

Bing Bai

Bing Bai is a PhD candidate (supervisors: Prof. Ben Zhong Tang and Prof. Zheng Zhao) at the School of Science and Engineering, The Chinese University of Hong Kong, Shenzhen, and the Guangdong Basic Research Center of Excellence for Aggregate Science. She received her BS degree in 2023 from the College of Chemistry, Zhengzhou University. Her research focuses on near-infrared II (NIR-II) fluorescence and cocrystal-based luminescent materials.

strong fluorescence in dilute solution but suffer from fluorescence quenching upon aggregation in the solid state, a phenomenon known as aggregation-caused quenching (ACQ).[3–5] This behavior severely limits their performance in optoelectronic applications such as organic light-emitting diodes (OLEDs).[6–8] In contrast, certain systems exhibit the opposite behavior: molecular monomers are non-emissive in the isolation state but become highly emissive in the aggregate state.[9,10] This effect, termed as aggregation-induced emission (AIE), was first reported by Tang's group in 2001,[11] who attributed the AIE phenomenon to the restriction of intramolecular motions (RIM) in the aggregate state.[12,13] These studies highlight that aggregate-state properties often arise from cooperative intermolecular effects and cannot be simply extrapolated from single-molecule characteristics. As such, molecular aggregates should be regarded as new functional entities. Investigating their behavior requires a conceptual shift beyond traditional reductionism. In recent years, aggregate science (also referred to as aggregology) has emerged as a multidisciplinary field dedicated to exploring the emergent properties and multiscale cooperative effects induced by molecular aggregation.[14,15] This holistic paradigm provides fundamental insights for the design and understanding of complex functional materials beyond the molecules.

Over the past century, the development of chemistry and materials science has predominantly followed the classical paradigm of ''designing molecules – synthesizing molecules – characterizing molecules – developing applications.'' This molecule-centered strategy has led to numerous landmark achievements, ranging from the structural optimization of pharmaceutical compounds to the development of high-performance organic optoelectronic materials, all of which rely on the precise tuning of molecular backbones, substituents, and conformations.[16–20] However, with the continuous advancement of research, the limitations of this paradigm have become increasingly evident. On the one hand, the molecular structure may not exhibit desired properties. On the other hand, the performance in the aggregate or solid state often deviates significantly from its behavior in the molecularly dispersed state. For example, many molecules with excellent photophysical properties in solution suffer from severe performance degradation in the aggregate state due to ACQ, thus limiting their applicability in real devices.

To address these challenges, researchers have gradually shifted their focus from isolated molecular properties to molecular aggregation behavior, bringing molecular crystal materials into the spotlight. Compared with dilute solutions or single-molecule systems, crystals offer three distinct advantages: (1) their long-range ordered structures can be precisely characterized by single-crystal X-ray diffraction (SXRD), providing a reliable foundation for establishing structure–property relationships,[21,22] (2) noncovalent intermolecular interactions (such as π–π stacking, hydrogen bonding, halogen bonding, and

Gian Albert Alfani

Gian Albert Alfani, born in Jakarta, Indonesia, is a PhD candidate (supervisor: Prof. Ben Zhong Tang) at the School of Science and Engineering, The Chinese University of Hong Kong, Shenzhen, and the Guangdong Basic Research Center of Excellence for Aggregate Science. He received his BS degree in 2023 from The Chinese University of Hong Kong, Shenzhen. His research focuses on the design of organic room-temperature phosphorescence (RTP) and circularly polarized luminescence (CPL) materials.

Zheng Zhao

Prof. Zheng Zhao is a Presidential Young Fellow at The Chinese University of Hong Kong, Shenzhen. He received his PhD from the Shanghai Institute of Organic Chemistry, Chinese Academy of Sciences in 2014, followed by postdoctoral research at The Hong Kong University of Science and Technology. He began his independent research at Southeast University in 2020 and joined CUHK-Shenzhen in 2021. His research focuses on functional aggregate materials, organic photosensitizers, and NIR-II luminescent systems for biomedical applications.

Ben Zhong Tang

Prof. Ben Zhong Tang received his BS and PhD degrees from the South China University of Technology and Kyoto University in 1982 and 1988, respectively. He conducted postdoctoral research at the University of Toronto in 1989–1994. He joined the Hong Kong University of Science and Technology in 1994 and was promoted to Chair Professor in 2008. He was elected to the Chinese Academy of Sciences in 2009 and the World Academy of Sciences for the Advancement of Science in Developing Countries in 2020. In 2021, he joined the Chinese University of Hong Kong, Shenzhen, as Dean of the School of Science and Engineering, with a concurrent appointment of X. Q. Deng Presidential Chair Professor.

charge transfer (CT)) can induce novel electronic structures and excited-state behaviors in crystals, thereby endowing the system with emergent properties,[23,24] (3) through crystal engineering strategies such as cocrystallization, self-assembly, or host–guest doping, one can modulate the material performance without altering the molecular backbone, effectively achieving "property tuning *via* packing" rather than through complex synthetic modifications.[25–27] For example, in organic electronic materials, cocrystallization with halogenated aromatics has been shown to significantly enhance the X-ray absorption and radiative conversion efficiency of conjugated luminophores, granting them scintillation properties without the need for heavy-atom substitution or complicated molecular design.[28–30] The incorporation of crystallization strategies not only provides solutions to the inherent limitations of traditional molecular design but also opens more feasible and versatile pathways for the development of functional materials.[31,32]

Molecular crystalline materials have demonstrated unique advantages in the field of functional materials in recent years, owing to the above advantages. Unlike single-molecule systems, the ordered alignment of molecules within crystals can induce entirely new properties, enabling applications in optoelectronics, biomedicine, and energy conversion systems.[33–36] In the context of luminescent materials, crystal engineering not only facilitates the stabilization of emission mechanisms that are difficult to achieve in traditional systems (*e.g.*, radical emission in triphenylmethyl radical crystals),[37,38] but also enables the precise tuning of excited-state processes through the design of intermolecular interactions, for example, enhanced intersystem crossing (ISC) resulting from spatial overlap of lone-pair electrons, thereby improving the phosphorescence efficiency of organic molecules.[39,40] Furthermore, donor–acceptor (D–A) type cocrystals can achieve tunable emission from the visible to near-infrared (NIR) region *via* controllable CT interactions, showing great promise in areas such as bioimaging and photothermal therapy.[41–43] More broadly, the ordered molecular packing in crystals supports multifunctional property integration: heavy-atom-containing cocrystals have emerged as candidates for novel organic X-ray scintillators due to their excellent X-ray absorption capabilities; mechanochromic luminescent crystals exhibit multicolor switching behavior through molecular rearrangement; and CT-based cocrystalline systems with effective charge separation mechanisms have been shown to enhance photothermal conversion efficiency.[44–46] These advances collectively highlight that precise control over molecular packing offers a powerful strategy not only to bypass the synthetic bottlenecks of complex molecule design, but also to significantly enhance or even endow new functionalities without altering the molecular structure itself, thereby establishing a new layer of material design logic beyond traditional structure–property relationships.

Materials science has long adhered to a reductionism paradigm; however, this mindset has been repeatedly challenged in practical applications. Molecular crystals, as highly ordered representatives of molecular aggregates, offer an ideal platform for redefining structure–property relationships.[47] In these systems, intermolecular interactions drive the aggregation process, and the aggregation pattern becomes a determining factor for the material properties. From radical emission to NIR luminescence and from X-ray responsiveness to photothermal conversion, the realization of these functions often does not rely on the molecular structure itself, but rather stems from aggregation-induced modulation of excited-state dynamics, energy transfer pathways, and electronic coupling.[48–51] Collectively, these observations emphasize that molecular aggregates should be regarded as distinct entities with their own intrinsic physicochemical characteristics. Through the integration of techniques such as SXRD, transient spectroscopy, and theoretical calculation, researchers are now trying to unravel structure–property relationships at the aggregate level.[52–54] In this context, aggregate science is rapidly emerging as a new core discipline alongside molecular science for understanding and constructing functional materials from a multiscale, collective perspective.

2. Single-component molecular crystals: packing-induced novel photophysical properties

According to conventional paradigms, the photophysical behavior of organic molecules has been regarded as a function of their intrinsic chemical structure. However, recent studies have revealed that even structurally simple single-component molecules can exhibit entirely new photophysical properties in the crystalline state, solely because of their specific molecular packing arrangements.[55–57] Unlike the random distribution of molecules in solution, the highly ordered alignment in crystals can profoundly influence excited-state processes through mechanisms such as steric hindrance, lone-pair electron interactions, and spontaneous stabilization of radical species ultimately giving rise to functions that are completely absent in the monomeric state.[58] These findings challenge the conventional paradigm of "structure determines property" and highlight the critical role of aggregation as an independent structural dimension. While the chemical structure forms the foundation of a molecule's photophysical behavior, the way molecules pack in the solid state is equally essential. Steric effects can effectively suppress non-radiative decay pathways; spatial interactions between lone-pair electrons can regulate ISC; and cooperative intermolecular forces can stabilize radical states.[59] Altogether, these mechanisms result in excited-state behaviors that are fundamentally distinct from those of isolated molecules. With the continuous advancement of crystal engineering, an increasing number of structurally simple organic molecules have been found to exhibit unique optical properties in the aggregate state, properties that are absent in dilute solutions. These discoveries not only break the linear relationship implied by the traditional structure–property paradigm but also offer a new theoretical foundation and practical approach for the development of photofunctional materials.

2.1 Emerging nonconjugated luminescent materials

According to established understanding, a π-conjugated framework has long been regarded as a prerequisite for constructing organic luminescent materials. However, recent studies have revealed that certain nonconjugated systems can also exhibit excellent emission properties in the aggregate state, a breakthrough that fundamentally challenges the traditional "no conjugation, no emission" design logic.[60–62] In these systems, the luminescence does not originate from intramolecular π-electron delocalization, but rather from excited states formed *via* noncovalent intermolecular or intramolecular interactions, such as spatial orbital coupling, n–n interactions between lone-pair electrons, and conformational locking effects.[63] These excitation pathways, formed by through-space interactions (TSIs), are nearly inaccessible in isolated molecules but become effectively activated in solid or nanoaggregate states, giving rise to unique optical behaviors such as AIE and clusteroluminescence (CL).[64,65] These findings not only broaden the structural scope of organic luminescent materials beyond conventional conjugated systems but also provide theoretical support for the design of highly efficient, structurally simple photofunctional materials.

A representative example of nonconjugated luminescent systems is the series of unique rotor-free rhodamine B-based AIEgens (BISX, ISX, MISX and MTSX) reported by Zhao and coworkers.[66] These molecules adopt an electronically nonconjugated structure in which the donor (D) xanthene and acceptor (A) isoquinolinone parts are connected by an sp^3-hybridized carbon bridge, thereby realizing a "conjugation-disrupted" electronic structure (Fig. 1a). Owing to the nearly orthogonal orientation of the D and A fragments, the charge transfer from

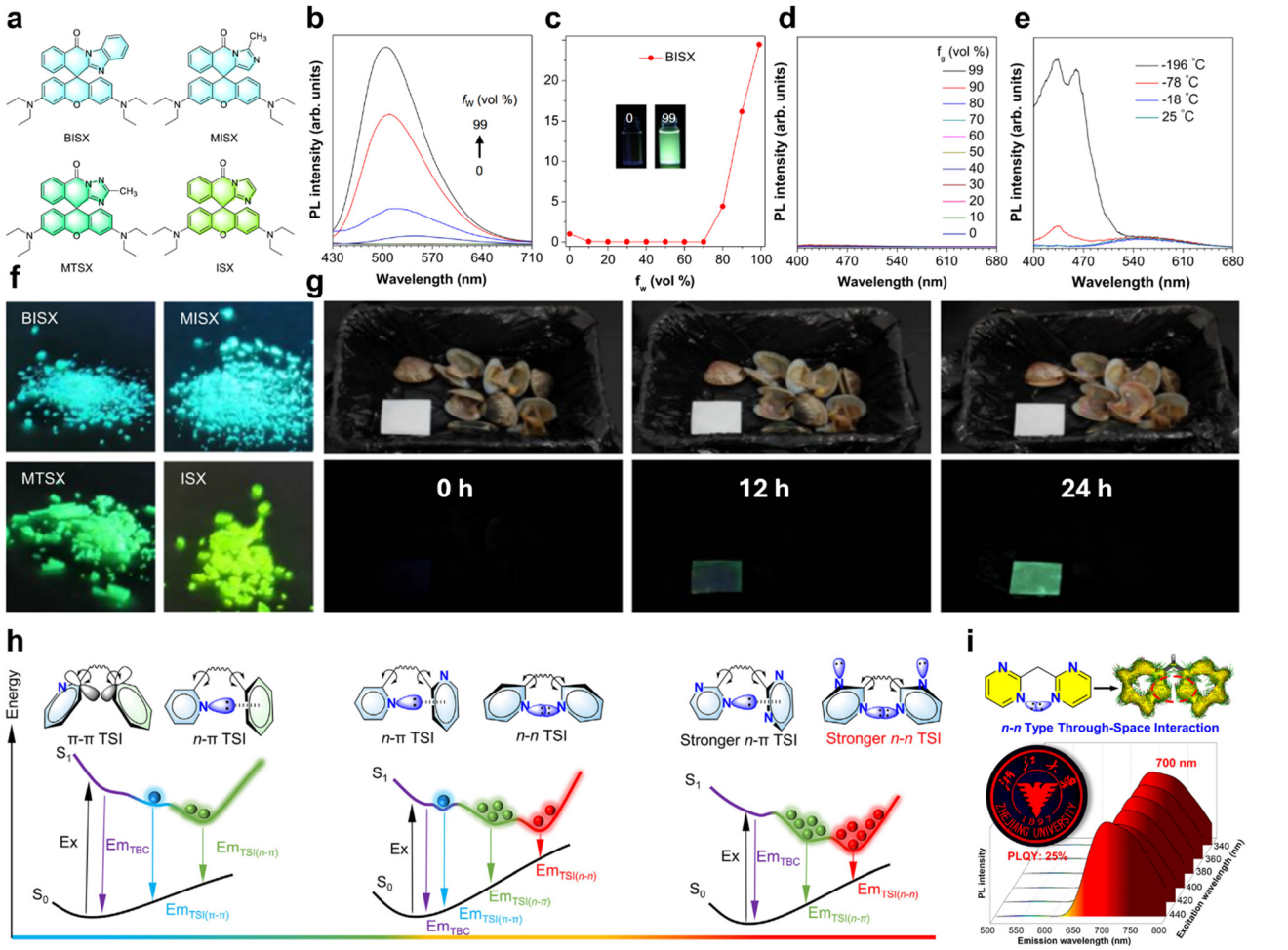

Fig. 1 Aggregation-induced conformationally driven emission changes in nonconjugated systems. (a) Molecular structures of rotor-free rhodamine B-based AIEgens (BISX, MISX, MTSX, and ISX). The filled colours correspond to their aggregate emission. (b) AIE behavior of BISX: PL spectra in THF/water mixtures with increasing water fractions (f_w). $c = 1 \times 10^{-5}$ M; λ_{ex} = 365 nm. (c) Plot of α_{AIE} (I/I_0) *versus* f_w. Inset: fluorescence images of BISX in f_w = 0% and 99%. (d) PL spectra of BISX in methanol/glycerol mixtures with different glycerol fractions (f_g). (e) Temperature-dependent PL spectra of BISX in THF at various temperatures. (f) Fluorescence images of BISX, MISX, MTSX, and ISX aggregates. (g) Biogenic amine detection *via* fluorescence changes in BISX-loaded sensors after clam exposure for 0, 12, and 24 h. Reproduced from ref. 66. Copyright © 2024, The Author(s), published by Springer Nature under a CC BY license. (h) Schematic energy diagrams showing different TSIs (π–π, n–π, and n–n) and their influence on emission in o-1Py-1Ph, o-2Py, and o-2Md. (i) Structure and AICD isosurface of o-2Md exhibiting sigma-type n–n TSI. Right: excitation-dependent PL spectra and fluorescence image at 365 nm. Reproduced with permission from ref. 67. Copyright © 2024, Elsevier Inc.

D to A (CT_{D-A}) excited states formed in solution is a forbidden state, resulting in negligible emission. However, in the aggregate or crystalline state, molecular conformational twisting significantly enhances the orbital overlap between D and A, converting the CT_{D-A} transition from a dark state into a transition-allowed excited state and consequently triggering strong fluorescence.

Taking BISX as an example, the molecule exhibits gradually intensified green fluorescence with increasing water fraction (f_w) in THF/water mixtures, and the photoluminescence (PL) intensity increases nearly 25-fold, displaying typical AIE behavior (Fig. 1b and c). To explore the underlying mechanism, the authors conducted both viscosity-dependent and temperature-dependent PL measurements (Fig. 1d and e). According to the classical RIM model, increasing solvent viscosity or decreasing temperature should suppress intramolecular motion and thereby enhance emission. However, BISX exhibited only marginal fluorescence changes under these conditions, suggesting that the emission was not primarily governed by the restriction of molecular rotation (RIR) or vibration (RIV). Instead, the observed fluorescence became significantly enhanced only when the molecules aggregated into the solid or crystalline state, which implies that conformational reorganization induced by aggregation plays a crucial role in activating the emissive pathway, rather than relying on the suppression of intramolecular motion alone. Based on these observations, the authors proposed "aggregation-induced molecular conformation change" as the dominant mechanism, wherein conformational rearrangement triggered by molecular packing fundamentally alters the nature of the excited state. In the aggregated state, these molecules generally exhibit stable and intense fluorescence (Fig. 1f) and demonstrate responsiveness to acidic and basic vapors, making them promising candidates for real-time monitoring of biogenic amine gas release (Fig. 1g).

Zhang and co-workers further aimed to elucidate the fundamental nature of excited-state formation in nonconjugated systems.[67] They established a structurally minimalist yet highly efficient through-space interaction-based database (TSI-based database) and systematically investigated how different types of TSIs govern excited-state behavior. Using a series of diarylmethane (DAM) derivatives as model compounds, the researchers designed three nonconjugated emitters with varying numbers of nitrogen atoms: o-1Py-1Ph (π–π TSI-dominated), o-2Py (n–π TSI-dominated), and o-2Md (n–n TSI-dominated) (Fig. 1h). With increasing heteroatom content and changes in spatial arrangement, the TSI type evolved from weak π–π TSI to strong n–n TSI. This transition was accompanied by enhanced orbital overlap in the excited state and a progressive redshift in the emission wavelength from 534 nm to 700 nm (Fig. 1i). Among them, o-2Md achieved a quantum yield as high as 25%, making it one of the smallest known nonconjugated near-infrared emissive molecules to date. To gain further insight into the nature of n–n TSI, anisotropy of the induced current density (AICD) isosurface analysis was employed. The results revealed that the excited-state electron density exhibited highly directional localized delocalization in space, which significantly facilitated excited-state formation. These n–n interactions possess the structural characteristics of σ-bond coupling while simultaneously exhibiting π-electron delocalization, providing an efficient mechanism for constructing excited states in nonconjugated systems.

In summary, the design of nonconjugated luminescent materials is no longer constrained by the requirement of a traditional π-conjugated backbone. Through the strategic introduction of TSIs, otherwise forbidden excited-state pathways can be effectively activated, enabling the development of structurally simple yet functionally superior optical materials. This emerging paradigm offers new design strategies for NIR light sources, sensors, and bioimaging applications, while also marking a conceptual shift from "structure–property" to "aggregation-excited-state construction".[68]

2.2 Lone-pair electron interactions in crystals

In recent years, increasing attention has been directed toward the role of lone-pair electrons in the regulation of excited states, particularly in organic molecular crystals containing heteroatoms (such as oxygen, nitrogen, and sulphur). The unique spatial distribution and orbital characteristics of lone pairs provide novel physical mechanisms for the generation and stabilization of triplet excitons.[48,69,70] In contrast to conventional strategies that rely on heavy atom effects to enhance spin–orbit coupling (SOC), lone-pair electrons can facilitate the construction of efficient ISC channels, thereby enabling room-temperature phosphorescence (RTP) emission under metal-free and dopant-free conditions.[71–74] Notably, when lone pairs are spatially confined within the molecular framework or crystal packing structure, they tend to form n–n or n–π types of through-space orbital coupling. This interaction can induce excited-state reorganization and enhance both the delocalization and lifetime of the triplet excitons. Further investigations have revealed that the synergistic interplay among molecular packing, heteroatom geometry, and crystal field effects collectively contributes to a lone pair-mediated multiple TSI mechanism.[75,76]

Zhao and co-workers systematically investigated the decisive role of lone-pair-electron-dominated multiple through-space interactions (TSIs) in excited-state regulation using a series of triarylamine-based molecular crystals.[77] The representative molecules (ToMeT, TpMoT, ToMoT-α, and ToMoT-β) were designed such that ToMoT-α and ToMoT-β exhibited folded conformations in their crystal structures, favouring the formation of multiple n–n and n–π TSIs. In contrast, ToMeT and TpMoT lacked effective pathways for spatial orbital coupling (Fig. 2c). In terms of photophysical behavior, the crystals of ToMeT and TpMoT displayed only short-lived bluish-violet fluorescence (λ_{em} = 359 and 405 nm) with total photoluminescence quantum yields (PLQYs) of 13.1% and 4.2%, respectively, and no RTP was observed (Fig. 2d and e). In sharp contrast, ToMoT-α and ToMoT-β exhibited persistent green phosphorescence ($\lambda_{em} \approx$ 540 nm) lasting over 1.5 seconds after the excitation source was turned off, with PLQYs of 16.1% and 19.0% and emission lifetimes of 204.6 ms and 216.9 ms, respectively (Fig. 2b, f and g), highlighting their excellent RTP performance. The marked differences in photophysical

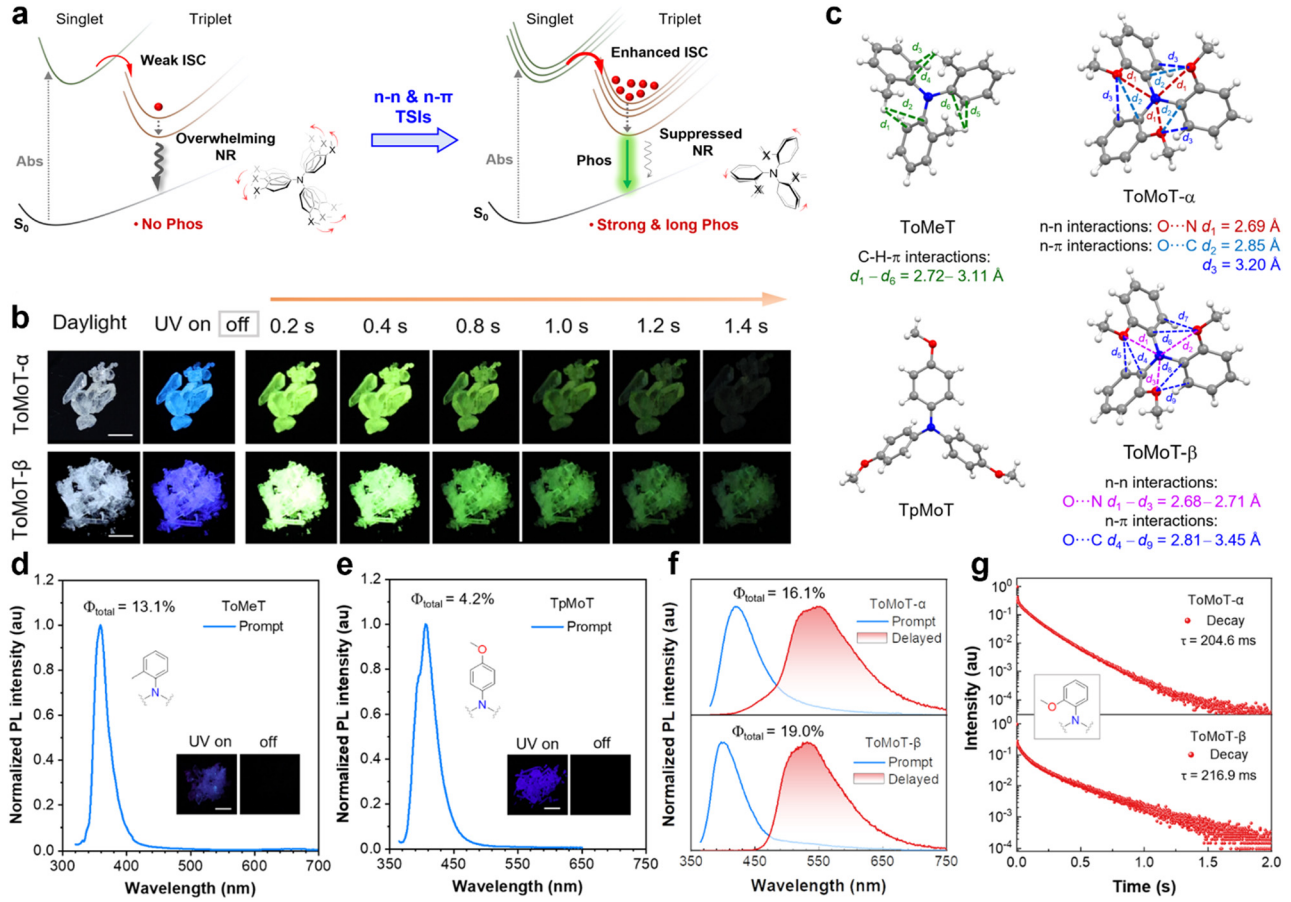

Fig. 2 Lone-pair-induced through-space interactions (TSIs) enable efficient room-temperature phosphorescence (RTP) in metal-free organic crystals by enhancing intersystem crossing (ISC) and suppressing nonradiative decay pathways. (a) Schematic illustration of the mechanism by which n–n and n–π TSIs facilitate ISC and promote long-lived phosphorescence, compared to systems lacking effective orbital overlap. (b) Photographs of ToMoT-α and ToMoT-β crystals under daylight, UV excitation (365 nm), and after UV is turned off, showing persistent green afterglow (scale bars = 0.5 cm). (c) Crystal structures of ToMeT, TpMoT, ToMoT-α, and ToMoT-β, highlighting the key noncovalent interactions: C–H···π in ToMeT; lack of orbital overlap in TpMoT; and multiple n–n and n–π interactions (*e.g.*, O···N, O···C) in ToMoT-α and ToMoT-β with distances ranging from 2.68 to 3.45 Å. (d) and (e) Prompt PL spectra of ToMeT (λ_{ex} = 300 nm) and TpMoT (λ_{ex} = 350 nm) crystals, showing short-lived fluorescence with total PLQYs of 13.1% and 4.2%, respectively. Insets: fluorescence images with 365 nm UV light on and off (scale bar = 0.5 cm). (f) Prompt and delayed (1 ms delay) PL spectra of ToMoT-α and ToMoT-β (λ_{ex} = 350 nm), demonstrating strong RTP with Φ_{total} = 16.1% and 19.0%, respectively. (g) Phosphorescence decay curves of ToMoT-α and ToMoT-β crystals, with long emission lifetimes of 204.6 ms and 216.9 ms. Reproduced with permission from ref. 77. Copyright 2025, American Chemical Society.

properties were primarily attributed to the spatial interactions induced by lone-pair electrons. In the ToMoT series, the *ortho*-methoxy oxygen atoms formed effective n–n (O···N, 2.68–2.71 Å) and n–π (O···C, 2.81–3.45 Å) interactions with the nitrogen or carbon atoms of the arylamine units. These interactions not only enhanced SOC but also rigidified the molecular backbone, thereby facilitating ISC and stabilizing the triplet state. In contrast, although ToMeT possesses an *ortho*-substituent, the methyl group lacks lone pairs and thus fails to establish TSIs, forming only weak C–H···π interactions, which do not contribute to through-space delocalization or triplet-state stabilization. While TpMoT contains methoxy groups, their *para*-positioned, planar configuration prevents effective spatial orbital overlaps, leading to insufficient excited-state reorganization and orbital coupling and consequently a lack of long-lived emission.

Despite the crystal systems of ToMoT-α ($Pa\bar{3}$) and ToMoT-β ($P\bar{1}$) being different, both exhibited outstanding RTP properties, demonstrating the generality and significance of lone-pair-driven TSI in triplet-state regulation. Lone-pair electrons not only promote electronic cloud delocalization between heteroatoms but also expand the number of ISC pathways through spatial orbital coupling, effectively suppressing non-radiative decay processes and prolonging emission lifetimes. This study provided the first systematic elucidation of the essential roles of n–n and n–π TSIs in triplet-state construction, offering a new theoretical foundation and molecular design strategy for metal-free organic RTP materials and delivering key insights into excited-state regulation in nonconjugated systems.

The critical role of lone-pair electrons in modulating excited-state behavior, especially in enabling efficient RTP in the absence of heavy atoms or metals, has opened a new avenue in material design. By facilitating n–n and n–π types of spatial orbital interactions, lone pairs significantly enhance ISC and triplet-state stability, overcoming the traditional dependence

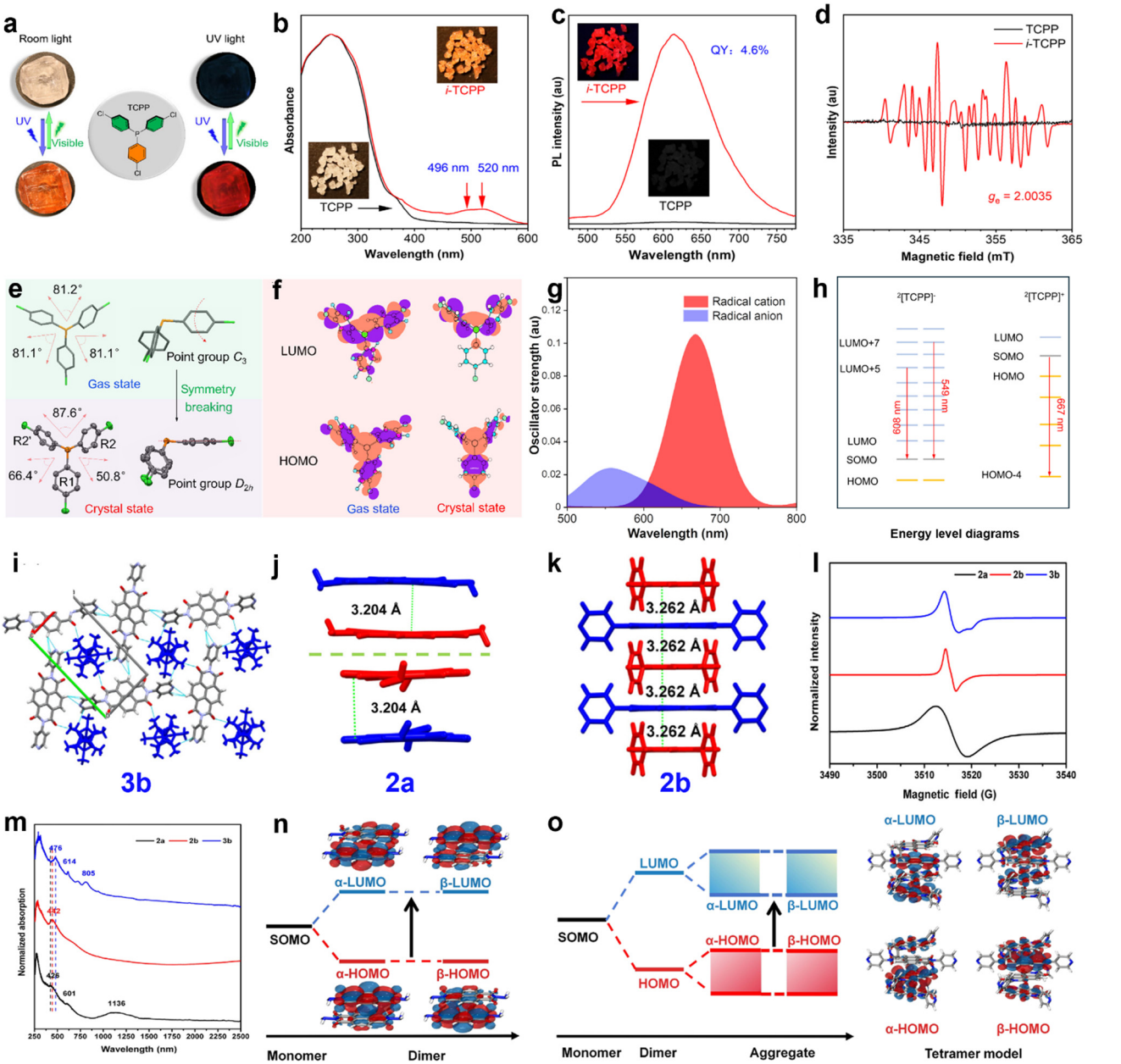

Fig. 3 Photoinduced stable radical generation and luminescence. (a) Schematic illustration of the reversible photochromic transformation of TCPP crystals into emissive radicals under UV light, exhibiting red luminescence upon irradiation and recovering under visible light. The molecular structure of TCPP is shown centrally. (b) UV-vis absorption spectra of TCPP crystals before and after UV exposure (λ_{ex} = 365 nm), with insets showing the corresponding appearance changes. (c) PL spectra of neutral and UV-activated TCPP (i-TCPP) crystals; quantum yield (QY) of the radical emission is 4.6%. Insets: Fluorescence photographs under UV excitation. (d) Electron paramagnetic resonance (EPR) spectra reveal a strong radical signal at g_e = 2.0035 for i-TCPP. (e) Comparison of the ground-state molecular geometries of TCPP in the gas phase and crystal phase, highlighting symmetry breaking from C_3 to D_{2h} due to intermolecular packing (DFT, BLYP/def2-SVP). (f) TD-DFT-calculated HOMO and LUMO orbitals of TCPP in gas and crystal states (M062X/def2-TZVP), showing enhanced charge delocalization in the crystal state. (g) Simulated oscillator strengths of radical cation and anion emissions (PBE0/def2-TZVP). (h) Frontier molecular orbital energy diagrams of the TCPP radical cation and anion (M062X/def2-TZVP), illustrating spin-orbital distributions in the excited state. Reproduced with permission from ref. 86. Copyright © 2021, Chinese Chemical Society. (i) Crystal packing diagram of radical 3b. (j) Side views of pairs of radical 2a viewed along the direction parallel to molecular long axis and short axis. (k) 1D π-stacking in 2b crystals, featuring a uniform intermolecular separation of 3.262 Å. (l) EPR spectra of 2a, 2b, and 3b radicals, indicating varying spin densities and packing effects. (m) Solid-state UV-vis-NIR absorption spectra of 2a, 2b, and 3b crystals embedded in KBr, showing distinct long-wavelength absorption features. (n) and (o) Schematic diagrams of SOMO-to-LUMO excitation in a 2a dimer (n) and 2b tetramer aggregate (o), based on UMN15/def2-TZVP calculations. Energy levels and spatial distributions of α/β HOMO and LUMO orbitals are shown. Reproduced with permission from ref. 58. Copyright © 2025, Chinese Chemical Society.

on heavy-atom-enhanced phosphorescence.[78,79] Studies on representative triarylamine molecular crystals illustrate that both the spatial arrangement and conformational rigidity of lone-pair donors dictate the strength of orbital overlap, thereby dramatically improving triplet-state lifetime and emission efficiency. This mechanism provides a theoretical basis for the development of next-generation metal-free RTP materials and broadens the designs for excited-state engineering.

2.3 Crystal-induced luminescence of organic radicals

Distinct from closed-shell systems, open-shell organic radicals with unpaired electrons have been considered intrinsically non-emissive, primarily due to their excited states being highly susceptible to quenching *via* non-radiative pathways. However, recent studies have revealed that certain structurally stable radicals, especially triarylmethyl derivatives, can exhibit appreciable fluorescence or even phosphorescence in the crystalline state.[80,81] In such systems, crystal environments not only suppress radical dimerization and spontaneous decomposition but also stabilize the excited state through intermolecular π–π stacking, spatial confinement, and orbital delocalization. This breakthrough highlights that crystal engineering provides not only physical protection for radical species but also a powerful means of tuning their photophysical behavior at the electronic-structure level, thereby expanding the scope of pure organic luminescent materials. With a deep understanding of radical emission mechanisms, these crystalline systems have demonstrated promising potential in optoelectronic devices, stimuli-responsive materials, and NIR imaging.[82–84] In the following section, representative systems will be discussed to elucidate the intrinsic correlations among molecular structure, crystal packing, and excited-state dynamics, emphasizing the physical origin and design strategies of crystallization induced radical luminescence.

Symmetry breaking, which refers to the loss of molecular symmetry induced by crystal packing and the resulting redistribution of electronic density that enables new transition pathways, has emerged as a powerful strategy for constructing new excited-state energy levels, particularly in open-shell organic radical systems where it provides a unique mode of excited-state regulation.[85] Zhao and co-workers demonstrated this principle through their study of tris(4-chlorophenyl)phosphine (TCPP) crystals, showing that light-induced radical luminescence originates from conformation-induced orbital separation and excited-state reconfiguration under crystalline constraints.[86] Upon ultraviolet irradiation, pristine TCPP crystals undergo a reversible transformation into a luminescent radical state (irradiated TCPP, i-TCPP), displaying stable red fluorescence and a clear photochromic response (Fig. 3a). This transformation forms a crystalline platform that stably supports radical emission in the open-shell state. This photoactivation process is first reflected in changes to the absorption profile: after UV irradiation, new absorption bands emerge at 496 and 520 nm, indicative of radical species formation (Fig. 3b). Simultaneously, the i-TCPP crystals exhibit bright red fluorescence under 365 nm excitation, with an emission maximum at $\lambda_{em} \approx 620$ nm and a photoluminescence quantum yield of 4.6% (Fig. 3c). Electron paramagnetic resonance (EPR) spectroscopy further confirms the generation of radical species, showing a g_e value of 2.0035, with the stability of the radicals being ensured by the crystalline environment (Fig. 3d).

The stabilization of the radical state arises from the structural reshaping imposed by crystal packing. In the gas phase, TCPP adopts a C_3-symmetric conformation, with the three phenyl rings equally spaced and exhibiting extensive electronic overlap (Fig. 3e, top). In this conformation, the HOMO and LUMO are spatially co-localized, resulting in limited excited-state separation and ineffective charge transfer. In contrast, the crystal structure induces a transformation to a D_{2h} symmetry, with large dihedral angle (87.6° and 50.8°) disparities between the phenyl rings, resulting in symmetry breaking (Fig. 3e, bottom). This symmetry distortion triggers orbital redistribution, as shown by TD-DFT calculations, with the HOMO and LUMO becoming localized on different aryl units in the crystalline state (Fig. 3f), wherein the energy and spatial distribution of molecular orbitals are reshaped by intermolecular interactions. This orbital separation enables a low-energy transition pathway for the radical species. Simulated emission spectra reveal that the TCPP radical cation exhibits red-region transitions centered around 667 nm with a significant transition dipole moment (Fig. 3g). Energy level analysis (Fig. 3h) further indicates that the dominant emission transition originates from HOMO−4 → SOMO, which represents a "cross-orbital excitation," in which the electron transition occurs between orbitals located on spatially distant parts of the molecule, rather than between conventional frontier orbitals. Compared with the radical anion, the spectral features of the radical cation more closely match experimental results, supporting its identity as the primary emissive species. This study elucidates a complete mechanistic pathway in which crystalline symmetry breaking drives HOMO–LUMO separation and orbital reconstruction, facilitating the formation of a stable photo-excited radical state that ultimately emits light. Throughout this process, structural distortion, charge separation, crystal stabilization, orbital reconfiguration, and transition selectivity act in concert to construct a multi-tiered control system for radical luminescence. The results provide a clear physical picture for the rational design of open-shell organic emitters.

In open-shell molecular systems, the stability of radical species and the structure of their excited states are governed not only by intrinsic electronic properties, but also by the packing arrangement in the crystalline state. Ma and co-workers systematically investigated this phenomenon by constructing three types of naphthalenediimide (NDI) anion radical crystals with distinct packing modes (monomer (3b), π-dimer (2a), and π-stack (2b)), revealing a cooperative mechanism by which crystal packing modulates radical orbital reorganization, spin coupling, and excitation behavior. In the monomeric crystal 3b, radical molecules form a two-dimensional array stabilized only by weak C–H···N and C–H···O interactions without any π–π contact (Fig. 3i).[58] As a result, the SOMO remains localized on individual molecules, representing a typical non-coupled open-shell configuration.

In contrast, in the 2a crystal, NDI radicals adopt a cofacial planar arrangement with a π–π distance of 3.204 Å (Fig. 3j), allowing substantial SOMO–SOMO overlap. This leads to electronic pairing between radicals and the formation of a two-electron multicentre excited unit. In 2b, the radicals are arranged in a one-dimensional π-stacked array (Fig. 3k); while the intermolecular coupling is weaker, the spatial continuity of orbital delocalization gives rise to a quasi-band-like electronic structure.

These packing-dependent effects manifest distinctly in the spectroscopic and magnetic properties. EPR spectra reveal that 3b exhibits sharp signals characteristic of isolated radicals, while both 2a and 2b show significantly attenuated signals, indicative of enhanced spin pairing. In particular, 2a displays clear signatures of antiferromagnetic coupling (Fig. 3l). Solid-state absorption spectra further confirm orbital reconfiguration: 3b absorbs in the UV-vis region, whereas 2a and 2b exhibit NIR absorptions at 1136 nm and >1500 nm, respectively (Fig. 3m), implying the formation of new excited-state configurations. Theoretical calculations indicate that in the π-dimer structure of 2a, the radical orbitals reorganize into an α-HOMO and β-LUMO pair, whose transition corresponds to the observed NIR emission (Fig. 3n). In 2b's π-tetramer configuration, coupling among four molecules results in four frontier orbitals (α/β-HOMO and α/β-LUMO), with reduced energy spacing and enhanced delocalization, endowing the system with greater excited-state flexibility (Fig. 3o). Thus, by modulating the SOMO distribution and coupling strength *via* crystal engineering, an evolutionary model emerges from localized monomeric radicals to coupled π-dimer and one-dimensional stacked states. This transformation not only reshapes the excited-state structure of radicals but also significantly influences their optical and magnetic responses, providing a theoretical and experimental framework for tuning radical functionalities through packing control.

Crystal structure plays a pivotal role in stabilizing radical luminescence. On one hand, crystallization physically isolates radicals and suppresses bimolecular reactions such as disproportionation and dimerization. On the other hand, by modulating molecular conformation, symmetry breaking, and packing arrangement, crystals alter the spatial distribution and coupling of radical orbitals. This facilitates orbital reorganization, charge separation, and energy-level restructuring, thereby enhancing the radiative transition efficiency and excited-state stability. Ordered packing motifs like π-dimers and π-stacks synergistically enable orbital delocalization and spin coupling, creating novel excited states in which non-emissive or weakly emissive radicals in solution exhibit strong and stable fluorescence or phosphorescence in the crystalline state. These findings not only challenge the conventional belief that open-shell organic materials are non-luminescent, but also provide critical structural guidelines and theoretical support for the rational design of radical-based pure organic optoelectronic materials. Simple organic molecules often exhibit photophysical behaviors in the crystalline state that are entirely absent in their isolated forms, owing to tight molecular packing and intermolecular interactions. In non-conjugated systems, aggregation leads to enhanced fluorescence through orbital localization and suppression of molecular vibrations, embodying the concept of "simple structure, complex performance" associated with aggregation-induced emission. For heteroatom-containing molecules with lone pairs, n···n and n···π orbital interactions significantly boost SOC and ISC efficiency, enabling efficient RTP without the need for heavy atoms. In open-shell radical systems, crystal packing induces conformational asymmetry and orbital reorganization, stabilizing the excited states and broadening the emission range of organic radicals. These findings underscore that aggregation is not merely a structural arrangement, but a fundamental dimension driving excited-state evolution and emergent functionalities. As crystal engineering techniques continue to advance, a deeper understanding of intermolecular orbital coupling will pave the way for a more universal structure–property regulation paradigm, accelerating the development of organic luminophores with enhanced efficiency, stability, and multifunctional integration.

3. Multicomponent molecular cocrystals: structure–function synergy through molecular co-assembly

Compared with single-component molecular crystals, multicomponent systems offer greater degrees of freedom in structural design and functional modulation. By introducing a second component to construct cocrystals, host–guest, or doped systems, these systems enable precise molecular-level control over conformational compatibility, energy-level alignment, and interaction pattern reorganization. As a result, the resulting crystals exhibit novel photophysical behaviors that surpass those of their single-component counterparts. In such systems, the abundance of noncovalent interactions (such as hydrogen bonding, π–π stacking, CT interactions, and spatial electrostatic forces) effectively couples multiple functional units, reshaping electron distributions and transition pathways in the excited state.[87] This in turn facilitates the coordinated regulation of critical parameters (such as emission wavelength, photothermal conversion efficiency, and excited-state lifetime). Specifically, cocrystals containing heavy atoms exhibit strong X-ray absorption and can efficiently convert high-energy radiation into visible-light scintillation, offering promising materials for high-resolution radiation detection. Donor–acceptor type crystals with strong CT characteristics allow for the construction of smaller energy gap, enabling NIR emission suitable for bioimaging and information transmission. In the context of photothermal conversion, ordered molecular packing and energy-level synergy significantly enhance nonradiative relaxation efficiency, allowing the crystal to heat rapidly under light irradiation, which has important implications for tumour photothermal therapy and solar energy harvesting.[88–90]

Overall, multicomponent molecular crystals, through structure–function co-design strategies, demonstrate significant advantages in expanding excited-state modulation pathways and integrating multiple energy-responsive mechanisms. Their outstanding performance across optical, electrical, and thermal

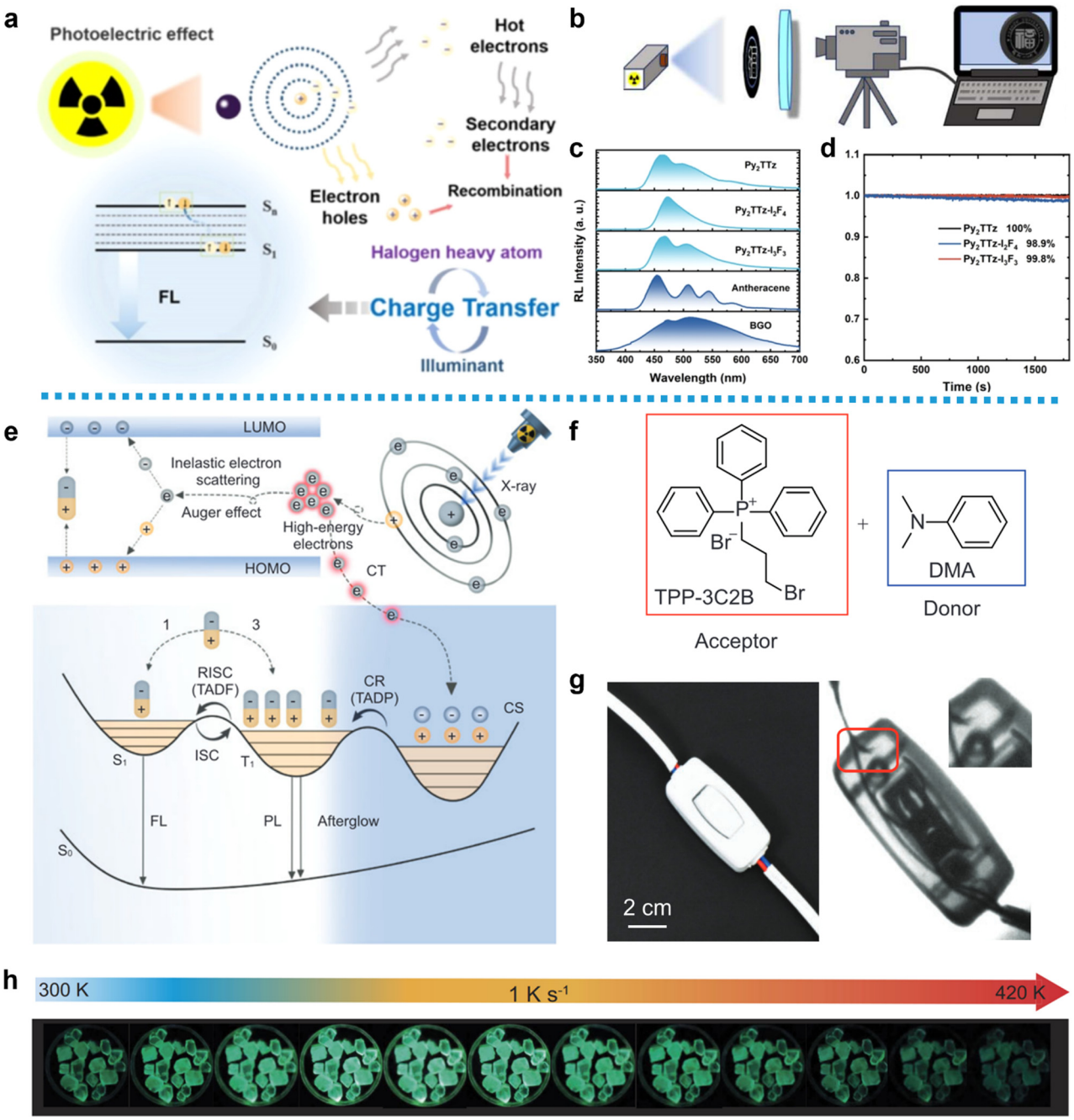

Fig. 4 X-ray excited luminescence (XEL) and scintillation mechanisms of organic cocrystals. (a) Illustration of the X-ray induced luminescence process based on the photoelectric effect and charge recombination, where halogen heavy atoms and donor–acceptor charge transfer states facilitate radiative de-excitation. (b) Schematic setup for X-ray imaging using an organic scintillator screen and CCD detection system. (c) Radioluminescence (RL) spectra of Py_2TTz, $Py_2TTz–I_2F_4$, $Py_2TTz-I_3F_3$, anthracene, and BGO crystals under X-ray irradiation at 278 mGy s^{-1} (50 kV, 79 mA), highlighting the enhanced emission of the iodinated cocrystals. (d) RL intensity stability of Py_2TTz-based materials under continuous X-ray irradiation for 1800 s, demonstrating high resistance to radiation-induced degradation. Reproduced with permission from ref. 101. Copyright © 2024, The Royal Society of Chemistry. (e) Energy diagram of the XEL process in TPP-3C2B:DMA, involving inelastic electron scattering, Auger electron generation, charge transfer (CT), intersystem crossing (ISC), reverse intersystem crossing (RISC), and delayed emission through thermally activated delayed phosphorescence (TADP). (f) Molecular structures of TPP-3C2B (acceptor) and *N*,*N*-dimethylaniline (DMA, donor), which co-crystallize into a radioluminescent organic complex. (g) Application of a TPP-3C2B:DMA scintillator for non-destructive X-ray inspection of a circuit switch, clearly revealing internal microcracks (highlighted in red). (h) Temperature-dependent luminescence photographs of TPP-3C2B:DMA from 300 K to 420 K at a heating rate of 1 K s^{-1}, demonstrating its potential for thermal sensing. Reproduced from ref. 102. Copyright © 2025, The Author(s). Published by Oxford University Press on behalf of China Science Publishing & Media Ltd under a CC BY license.

domains positions them as promising candidates for high-performance, multifunctional material platforms in advanced applications.

3.1 Cocrystal X-ray scintillators

X-ray scintillators are functional materials capable of efficiently converting high-energy X-ray photons into low-energy visible light and are widely used in medical imaging, security inspection, nondestructive testing, and high-energy physics detection.[91–95] Achieving high-performance scintillation typically requires the simultaneous fulfillment of multiple criteria, including strong X-ray absorption, high radiative conversion efficiency, rapid response time, and excellent spatial resolution. Although conventional inorganic scintillators (such as LuAG, CsI, and BaF_2) offer outstanding performance, their inherent drawbacks, including high-temperature synthesis, mechanical brittleness, and poor flexibility, significantly hinder their integration into flexible electronics and portable imaging systems.[96–98] In this context, the development of pure organic scintillators with both high performance and good processability has emerged as a frontier research direction. Cocrystal engineering provides a feasible and effective strategy for constructing efficient organic scintillators. By co-crystallizing highly emissive π-conjugated fluorophores with auxiliary components containing high atomic number (high-*Z*) elements, it is possible to establish a synergistic system within the crystal lattice that enables efficient energy conversion from X-ray absorption and excited-state generation to visible-light emission. The high-*Z* components, due to their strong photoelectric absorption capabilities, generate high-energy electron–hole pairs upon X-ray irradiation. These charge carriers are then rapidly transferred along the well-defined energy transport pathways constructed within the cocrystal to the organic emitting centers, where they recombine and emit light in the form of fluorescence or phosphorescence. This synergistic mechanism not only significantly enhances scintillation efficiency but also offers structural tunability for regulating emission wavelength, intensity, and response time.[99,100]

Lin and co-workers developed a charge-transfer-type organic scintillator system *via* a cocrystallization strategy by introducing high-*Z* halogen elements. The system was constructed using 2,5-di(4-pyridyl)thiazolo[5,4-*d*]thiazole (Py_2TTz) as the donor matrix and 1,4-diiodotetrafluorobenzene (I_2F_4B) or 1,3,5-trifluoro-2,4,6-triiodobenzene (I_3F_3B) as acceptors.[101] In the resulting cocrystals, the halogen-bond-driven D–A stacking structure not only stabilized the molecular arrangement but also significantly enhanced X-ray absorption capability and excited-state energy transfer efficiency. The excitation mechanism involves X-ray-induced photoionization, generation of electron–hole pairs, secondary electron recombination, excited-state formation, and SOC enhanced energy transfer, ultimately leading to efficient visible-light emission (Fig. 4a). At the device level, imaging systems based on these cocrystal materials generated digital images with high structural clarity and sharp edges, demonstrating their application potential in high-resolution X-ray detection (Fig. 4b). In terms of radioluminescence (RL) performance, the Py_2TTz–I_2F_4 cocrystal exhibited stronger emission intensity and a narrower bandwidth with a full width at half maximum (FWHM) of 52 nm, compared to both the single-component Py_2TTz and the traditional inorganic scintillator BGO. Notably, its maximum RL signal reached 1.46 times that of BGO, highlighting the remarkable energy conversion efficiency conferred by the cocrystal structure (Fig. 4c). Moreover, the system exhibited exceptional radiation resistance, with emission retention rates of 98.9% for Py_2TTz–I_2F_4 and 99.8% for Py_2TTz-I_3F_3 after continuous irradiation for 1800 s, reflecting excellent structural stability and photophysical reliability (Fig. 4d).

Zang and co-workers further developed an organic X-ray detection material that simultaneously exhibits room-temperature scintillation and thermally activated delayed phosphorescence (TADP) by constructing a cocrystal composed of halogenated triphenylphosphonium cations (TPP-3C2B) and a minor amount (0.5 mol%) of the electron donor DMA.[102] Within this cocrystalline structure, the extremely low doping level of DMA induced a stable charge separated (CS) state. Upon X-ray excitation, the system undergoes high-energy electron–hole pair generation, inelastic scattering, auger processes, and intermolecular charge transfer, ultimately producing T_1 excitons that emit fluorescence, phosphorescence, and afterglow (Fig. 4e). Despite its low concentration, DMA effectively introduces trap states without disrupting the ordered lattice of the host crystal, thereby enabling thermal control of the excited-state processes (Fig. 4f). The resulting scintillation screen was capable of accurately identifying minute defects in complex electronic circuitry with sharp edge contrast and a high signal-to-noise ratio, demonstrating strong potential for nondestructive testing applications (Fig. 4g). Moreover, across a temperature range of 300–420 K, the material continuously emitted visible light under thermal stimulation, independent of external light sources, displaying characteristic TADP behavior and offering temperature-responsive functionality for flexible, low-dose radiation detection (Fig. 4h).

In summary, the above studies systematically demonstrate the unique advantages of multicomponent cocrystal strategies in enhancing organic scintillation performance. By introducing high-*Z* acceptors and other electron donors and leveraging precisely controlled molecular packing within the crystal lattice, the traditionally incompatible properties of X-ray absorption and delayed emission in organic systems are synergistically integrated into a single material. This strategy not only significantly expands the functional scope of purely organic materials for high-energy radiation conversion, but also profoundly elucidates at the structure-excited state coupling level, the central role of aggregate state engineering in regulating complex excitation processes.

3.2 Cocrystal NIR materials

Near-infrared (NIR) luminescent materials hold great promise for applications in biological imaging, disease diagnosis, night vision and information security, owing to their deep tissue penetration, minimal autofluorescence interference, and long-range signal transmission.[103–106] However, to achieve efficient NIR emission, organic materials need to have a small energy gap (S_1–S_0 gap), but this often leads to enhanced vibrational dissipation and decreased excited state stability, which in turn severely limits the PLQY and lifetime of the material. To

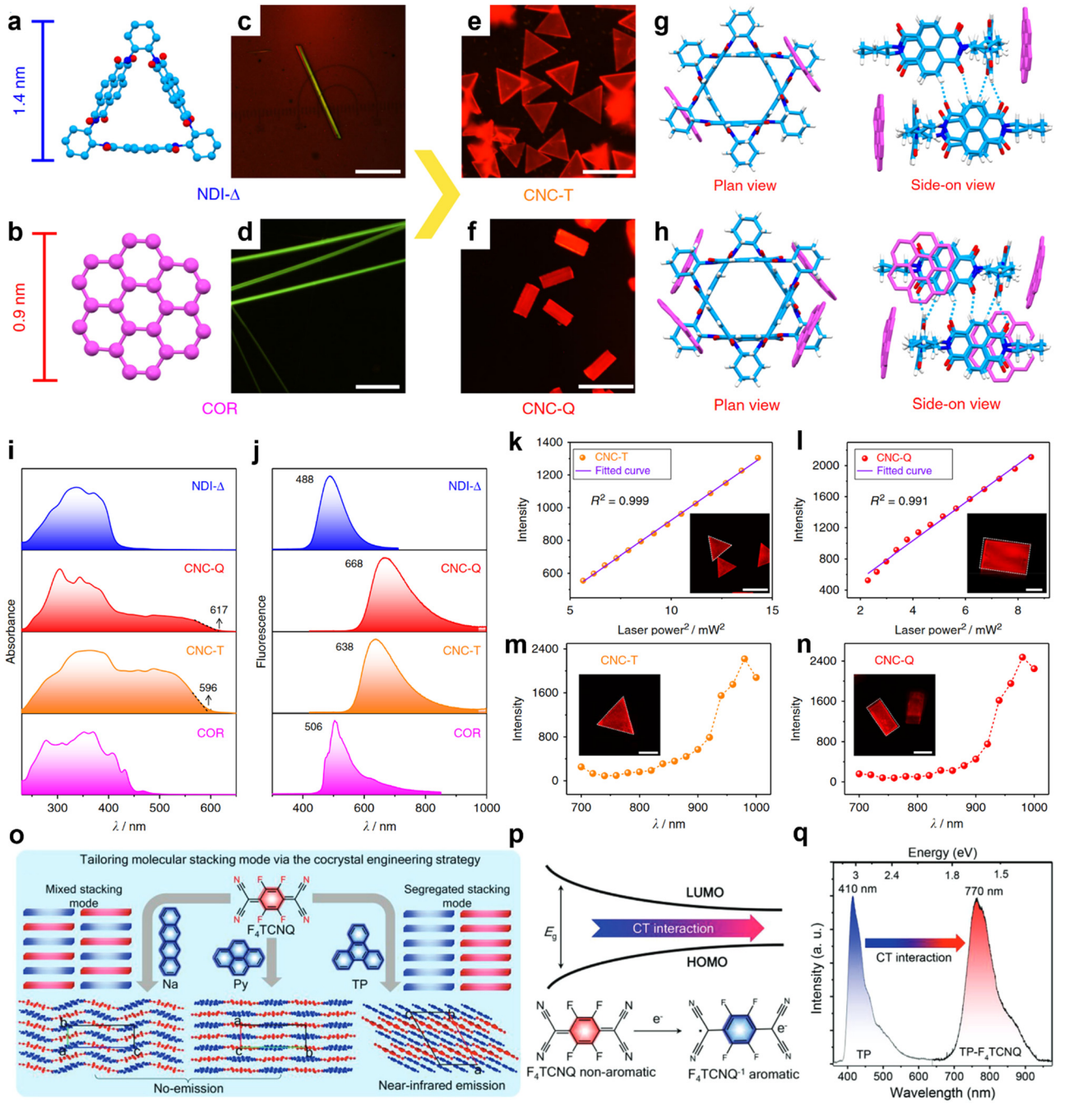

Fig. 5 Donor–acceptor cocrystals for red-shifted and two-photon responsive near-infrared emission. (a) and (b) Molecular structures and dimensions of NDI-Δ (light blue: C; dark blue: N; red: O) and COR (pink: C). (c) and (d) Fluorescence microscopy images of needle-like NDI-Δ and COR crystals showing green emission. Scale bars: 20 μm and 40 μm, respectively. (e) and (f) Fluorescence microscopy images of cocrystals CNC-T (triangular) and CNC-Q (quadrangular), both exhibiting red luminescence. Scale bar: 50 μm. (g) and (h) Molecular packing diagrams (plane and side views) of CNC-T and CNC-Q, demonstrating distinct face-to-face π–π stacking interactions between NDI-Δ and COR components in the solid state. (i) and (j) Solid-state absorption and fluorescence spectra of NDI-Δ, CNC-Q, CNC-T, and COR, where cocrystals exhibit pronounced red-shifted emissions due to charge-transfer (CT) interactions. (k) and (l) Laser power-dependent two-photon excited fluorescence intensity of CNC-T and CNC-Q (λ_{ex} = 1000 nm), fitted with quadratic relationships ($R^2 > 0.99$). Insets: two-photon fluorescence images; scale bars: 20 μm and 50 μm, respectively. (m) and (n) Two-photon emission spectra of CNC-T and CNC-Q collected from marked regions in (k) and (l). Reproduced from ref. 110. Copyright © 2020, The Author(s). Published by Springer Nature under a CC BY license. (o) Self-assembly strategy for CT cocrystals with varying stacking motifs, where TP–F_4TCNQ adopts segregated stacking yielding NIR emission, while Na–F_4TCNQ and Py–F_4TCNQ show mixed packing and are non-emissive. (p) Schematic energy diagrams illustrating HOMO–LUMO evolution and electron transfer from the donor to acceptor, leading to radical stabilization *via* TCNQ reduction. (q) Steady-state photoluminescence spectra of TP and TP–F_4TCNQ, showing a dramatic red shift upon cocrystallization due to enhanced CT interaction. Reproduced with permission from ref. 111. Copyright © 2022, Wiley-VCH.

overcome the inherent trade-off between quantum efficiency and excited-state stability in traditional organic NIR emitters, cocrystal systems based on cocrystal engineering offer an effective route for structure–function co-optimization.[107] By co-crystallizing donor and acceptor molecules and utilizing intermolecular charge transfer to guide excited-state modulation, the energy gap between S_1 and S_0 can be effectively narrowed, resulting in red-shifted emission.[108,109] Simultaneously, the ordered molecular packing within the crystal suppresses high-frequency vibrational coupling, thereby reducing non-radiative decay and significantly prolonging excited-state lifetimes while enhancing emission efficiency. Compared with conventional single-component molecular crystals, these multicomponent cocrystalline systems not only integrate the optoelectronic features of individual components but also induce steady-state NIR emission behaviors that are otherwise absent in single-component systems through ordered aggregation. This strategy opens new avenues for constructing high-performance NIR materials.

Stoddart's group developed a cocrystal system composed of the electron acceptor naphthalenediimide-based triangle (NDI-Δ) and the donor coronene (COR), resulting in organic crystalline materials that exhibit both NIR emission and two-photon responsive properties.[110] The NDI-Δ molecule features a rigid triangular core and terminal aromatic rings, maintaining a twisted conformation conducive to enhanced orbital delocalization. COR is a conjugated aromatic donor with favorable π-electronic characteristics. The two molecules show excellent compatibility in spatial dimensions, charge distribution, and π-orbital symmetry, making them ideal for forming compact donor–acceptor (D–A) stacked assemblies (Fig. 5a and b). By tuning the crystallization conditions and molar ratios, two types of COR–NDI-Δ co-crystals (CNCs) with triangular and quadrangular morphologies, denoted as CNC-T and CNC-Q respectively, were successfully prepared. They displayed triangular and rectangular morphologies, respectively, and their emission shifted from the green fluorescence of the parent single crystals to prominent red fluorescence, reflecting reconstructed excited-state energy levels and altered charge-transfer (CT) behavior (Fig. 5c–f). SXRD revealed that both CNC-T and CNC-Q adopt face-to-face π–π stacking to form stable D–A CT complexes. In CNC-T, COR and NDI-Δ alternate layer-by-layer in a 1 : 1 ratio, forming a symmetric sandwich-like arrangement that facilitates regular CT pathways. CNC-Q, by contrast, exhibits slip-stacked π–π interactions with increased overlap area and stronger electronic coupling, significantly enhancing the stability of the CT state (Fig. 5g and h). These differences in molecular packing directly impact the spatial distribution of the HOMO and LUMO and the degree of energy level splitting. As a result, CNC-T and CNC-Q show markedly reduced bandgaps compared to NDI-Δ and COR, with emission peaks redshifted to 638 nm and 668 nm, respectively, falling in the deep red to NIR region (Fig. 5i and j). Two-photon excitation experiments further demonstrate that under 1000 nm laser irradiation, both CNC-T and CNC-Q exhibit efficient upconverted fluorescence, with emission intensity showing a quadratic dependence on laser power, confirming a standard two-photon absorption (TPA) process (Fig. 5k and l). Their two-photon emission spectra span the 700–900 nm range, attributed to the cocrystal-induced CT state, which maintains excellent excited-state lifetime and radiative efficiency under nonlinear excitation (Fig. 5m and n). Theoretically, this strong two-photon response arises from the stabilized CT state within the cocrystal, which suppresses non-radiative decay, enhances excited-state coupling symmetry, and increases both the transition dipole moment and multiphoton cross-section.

By rationally designing the cocrystal stacking of D–A molecules, Liao and co-workers constructed a TP–F_4TCNQ cocrystal composed of triphenylene (TP) and 2,3,5,6-tetrafluoro-7,7,8,8-tetracyanoquinodimethane (F_4TCNQ), which successfully exhibited intense NIR emission at 770 nm along with excellent optical waveguide properties.[111] A systematic comparison of cocrystals based on different donors, naphthacene (Na), pyrene (Py), and TP with F_4TCNQ revealed that TP–F_4TCNQ adopted a segregated stacking mode, whereas Na–F_4TCNQ and Py–F_4TCNQ formed mixed-stack structures. In the segregated arrangement, TP and F_4TCNQ independently assemble into separate columnar stacks. This face-to-face π–π stacking, reinforced by intermolecular hydrogen bonding, forms an ordered crystalline network that effectively suppresses nonradiative decay caused by molecular vibrations, thereby enhancing the stability and efficiency of the excited state (Fig. 5o). From the perspective of excited-state processes, the electronic transition in TP–F_4TCNQ mainly occurs between the HOMO of TP and the LUMO of F_4TCNQ, generating a stable CT state. Upon accepting electrons, F_4TCNQ is reduced to its aromatic radical anion form (F_4TCNQ^-), giving rise to a CT emission band at 770 nm, which is significantly red-shifted compared to the blue emission of pristine TP (410 nm) (Fig. 5q). Theoretical calculations and experimental results revealed that the degree of charge transfer in TP–F_4TCNQ is only 0.00103, markedly lower than that in Py–F_4TCNQ (0.01850). This weak CT character enhances transition allowedness and radiative efficiency, effectively overcoming the emission-forbidden nature typically associated with strong CT states (Fig. 5p). Additionally, the $\sim 40^\circ$ dihedral angle between donor and acceptor molecules in the cocrystal limits π-conjugation extension, promoting excited-state localization and radiative decay enhancement.

Through cocrystal engineering of D–A systems, organic crystalline NIR materials achieve synergistic improvements in emission wavelength, excited-state lifetime, and nonlinear optical response. Intermolecular charge transfer reduces the S_1–S_0 energy gap, while ordered molecular packing enhances orbital coupling and suppresses nonradiative decay caused by high-frequency vibrations. Specifically, strong CT-state systems exhibit prominent emission redshifts and two-photon responsiveness, whereas weak CT-state systems retain strong transition allowedness and excited-state stability to achieve efficient NIR luminescence. Compared to single-component crystals, cocrystal systems offer richer structural tunability and excited-state regulation pathways, enabling a systematic strategy from molecular packing to NIR functional output. This lays

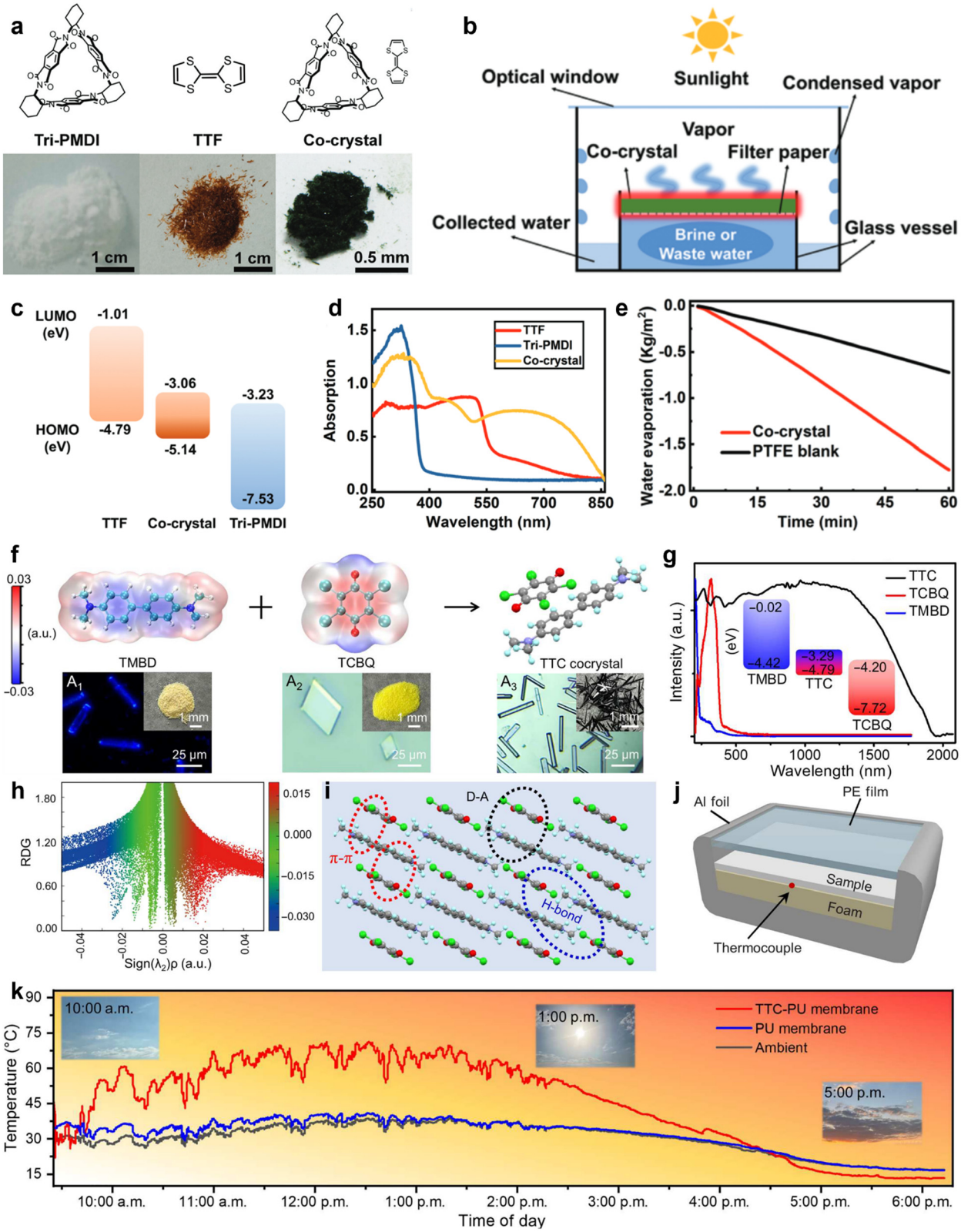

Fig. 6 Donor–acceptor cocrystallization enables enhanced broadband light absorption and efficient photothermal conversion. (a) Molecular structures of TTF, Tri-PMDI, and their charge-transfer cocrystals, along with photographs of corresponding powders. (b) Schematic diagram illustrating the setup for solar-driven water evaporation using the cocrystal membrane. (c) Calculated HOMO–LUMO energy levels of individual molecules and their cocrystals, showing reduced energy gap upon cocrystallization. (d) UV-vis absorption spectra of TTF, Tri-PMDI, and their cocrystals, highlighting enhanced broadband absorption in the co-crystal. (e) Time-dependent water evaporation rates under sunlight for the cocrystal membrane *versus* PTFE control, demonstrating superior solar steam performance of the cocrystal. Reproduced with permission from ref. 44. Copyright © 2020, The Royal Society of

Chemistry. (f) Electrostatic potential (ESP) surfaces and cocrystal formation of TMBD and TCBQ into TTC cocrystals, with FM and optical images of respective powders and TTC cocrystal microrods. Scale bars: 1 mm (powders) and 25 μm (crystals). (g) UV-vis-NIR absorption spectra of TMBD, TCBQ, and TTC cocrystal microrods; inset: frontier orbital energy levels indicating strong charge-transfer characteristics in the cocrystal. (h) Reduced density gradient (RDG) analysis of TTC cocrystals, illustrating weak non-covalent interactions that facilitate ordered stacking. (i) Crystal packing of TTC cocrystal microrods, with visualized π−π stacking, hydrogen bonding, and D–A interactions. (j) Schematic representation of the setup used to evaluate outdoor photothermal performance. (k) Real-time temperature tracking of the TTC–PU membrane, pristine PU membrane, and ambient environment under natural sunlight exposure, confirming efficient photothermal conversion of the cocrystal composite. Reproduced from ref. 112. Copyright © 2023, The Authors, licensed by AAAS under a Creative Commons Attribution-NonCommercial (CC BY-NC 4.0) license.

a solid theoretical foundation and design paradigm for the development of high-efficiency, tunable organic crystalline NIR emitters.

3.3 Cocrystal photothermal materials

To achieve efficient and sustainable photothermal conversion performance, multicomponent crystalline materials developed *via* cocrystal engineering provide a structurally tunable platform superior to conventional single-component systems. By employing cocrystallization or host–guest doping strategies, efficient nonradiative decay channels can be introduced at the crystal level, while simultaneously modulating the localization of the excited states, energy level distribution, and thermal vibration modes. These features significantly enhance photothermal responsiveness and stability under solid-state conditions. Particularly in solar-driven seawater desalination and precise photothermal therapy applications, such materials leverage intermolecular interactions to cooperatively optimize the dissipation pathways of excited states.[113–116] This approach overcomes inherent limitations in single-component systems, such as ACQ or insufficient heat dissipation. As a result, a tightly coupled structure-excited-state-thermal conversion functional network is established, enabling robust and high-performance photothermal behavior.

Zhao and co-workers developed a cocrystal system based on CT interactions, achieving efficient and stable NIR photothermal conversion.[44] The researchers selected the triangular electron acceptor cyclic trimeric pyromellitic diimide (Tri-PMDI) and planar donor molecule tetrathiafulvalene (TTF) to self-assemble into an ordered cocrystal structure, significantly altering the material's electronic structure and excited-state behavior (Fig. 6a). Tri-PMDI features high geometric rigidity and symmetry, providing a stable spatial framework for constructing well-ordered two-dimensional layered structures. Strong D–A interactions between Tri-PMDI and TTF induce pronounced charge transfer, narrowing the HOMO–LUMO bandgap to approximately 2.08 eV (Fig. 6c) and generating broad NIR absorption in the 700–850 nm range (Fig. 6d). The cocrystal forms dense π–π stacking and multiple noncovalent interactions, establishing tight electronic coupling channels that enhance excited-state localization and suppress radiative decay. As a result, the absorbed photon energy is predominantly released in the form of heat. Under sunlight irradiation, the cocrystal film rapidly heats up and drives interfacial water evaporation (Fig. 6b). In practical freshwater evaporation tests, the cocrystal film achieves significantly higher evaporated mass within 60 minutes compared to the blank polytetrafluoroethylene (PTFE) membrane (Fig. 6e), confirming its superior photothermal conversion efficiency. Its broad-spectrum absorption, combined with efficient CT-state-induced nonradiative dissipation, enables thermal conversion far exceeding that of conventional organic materials in the solid state.

Zhuo and co-workers further introduced electrostatic potential modulation and intermolecular noncovalent interaction analysis to design a class of structurally ordered, thermally responsive elastic cocrystal photothermal materials.[112] Unlike the systems focused on macroscopic thermal effects, this study centers on the microscopic regulation of energy dissipation pathways through charge distribution and crystal packing, thereby expanding the structure–function understanding of multicomponent crystalline materials. They constructed a CT-based cocrystal system by co-assembling a strong electron donor, *N*,*N*,*N*′,*N*′-tetramethylbenzidine (TMBD), with a chlorine-rich acceptor, tetrachloro-1,4benzoquinone (TCBQ), forming the TMBD–TCBQ (TTC) cocrystal. Charge density analysis revealed a distinct electrostatic potential gradient between molecules in TTC, which drives a stable and efficient charge transfer process (Fig. 6f). Spectroscopic characterization further confirmed significantly enhanced absorption in the NIR region, and band structure calculations revealed increased asymmetry in electronic transitions, favoring nonradiative relaxation (Fig. 6g). RDG analysis and crystal packing results indicated that the cocrystal adopts a continuous π–π stacking and finely distributed nonbonding interaction network, which collectively provide robust dissipation channels in the excited state, effectively suppressing thermal energy loss (Fig. 6h and i). In practical tests, TTC was fabricated into a polyurethane (PU) composite film (TTC–PU), which exhibited pronounced temperature elevation under natural sunlight, greatly outperforming both the pure polymer film and the undoped system, highlighting its application potential in solar-driven thermal management (Fig. 6j and k).

Overall, the performance enhancement of photothermal crystalline materials relies on the effective synergy of energy absorption, transfer, and nonradiative dissipation pathways. Cocrystal systems construct efficient excited-state channels through intermolecular CT, thereby broadening the light absorption range and improving photothermal conversion efficiency. Coupled with ordered crystal packing and electrostatic potential regulation, these systems enable spatial localization of excited-state energy and multipath dissipation, significantly enhancing thermal stability and photothermal responsiveness in the solid state. Compared with traditional single-component systems, such multicomponent crystalline materials exhibit a high degree of structural tunability, mechanistic design flexibility, and functional coupling, providing both theoretical foundations and engineering strategies for the next generation of high-performance photothermal conversion platforms.

Multicomponent molecular crystals, governed by noncovalent interactions such as hydrogen bonding, π–π stacking, and halogen bonding, enable ordered cooperation among different components, thereby endowing the crystalline assemblies with unique photophysical properties that surpass those of the individual constituents. Within the crystal lattice, functional units achieve conformational complementarity and energy-level alignment, forming cooperative systems that modulate the generation, transformation, and emission of excited states. For instance, cocrystals formed by combining heavy-atom-containing components with emissive building blocks exhibit efficient X-ray-to-visible energy conversion under irradiation. D–A systems with strong orbital overlap and CT interactions give rise to high-performance NIR luminescence, while the introduction of energy traps or enhanced nonradiative pathways can markedly improve photothermal conversion efficiency. Compared with traditional approaches that rely on covalent modifications, the cocrystal strategy allows for structural and functional integration in the aggregated state without altering the molecular skeletons, relying instead on intermolecular complementarity. This construction method not only offers excellent tunability and generality but also provides a flexible and efficient route for the development of high-performance, multifunctional organic optoelectronic materials.

4. Conclusion and outlook

In recent years, molecular aggregates, particularly organic crystals, have garnered increasing attention as photofunctional materials. This growing interest reflects a fundamental paradigm shift: material properties are no longer regarded as solely determined by individual molecular structures, but are increasingly understood as emergent phenomena arising from intermolecular interactions and collective aggregation. Notably, the optoelectronic behaviors observed in dilute solutions or gas-phase monomers often fail to predict those exhibited in aggregate or crystalline states. This deviation from a monomer-centric view toward the investigation of collective effects lies at the heart of aggregate science, which is underpinned by the principles of "more is different," "0–1," and "1 + 1 > 2."[117] That is, when molecules assemble into aggregates *via* noncovalent interactions, they can exhibit entirely new or enhanced properties that transcend the intrinsic characteristics of single molecules.

From this perspective, molecular crystals function not merely as spatial assembly for monomers, but as integrated platforms for emergent function. In crystalline systems, the structure–property relationship gives rise to higher-order cooperative phenomena governed by molecular conformation, symmetry, and intermolecular interactions. Orbital overlap, charge transfer, π–π stacking, and hydrogen-bonding networks act synergistically to modulate excited-state dynamics enhancing energy transfer efficiency, prolonging excited-state lifetimes, and enabling unique phenomena such as RTP and crystallization-induced emission enhancement (CIEE), which are typically inaccessible in dilute solutions.[118,119] Consequently, crystallization and cocrystal engineering provide indispensable strategies for fine-tuning luminescence properties, stabilizing excited states, constructing optical waveguides, and designing tailored energy dissipation pathways.[120–124] Beyond enhancing individual properties, molecular crystals enable the integrated expression of optical, electronic, and magnetic functions through cooperative intermolecular interactions. For example, D–A assemblies can stabilize CT states and trigger multi-physical responses, such as coupled optical, thermal, and electrical behaviors. These emergent effects vividly illustrate the essence of aggregate science where ordered molecular architectures unlock synergistic functionalities unattainable in disordered phases.

Despite these advances, several challenges remain. The trade-off between solid-state luminescence efficiency and processability continues to limit practical applications, particularly in flexible devices. In addition, accurately predicting aggregate-state properties from single-molecule structures remains difficult due to the complex interplay of packing, conformation, and environment. These unresolved issues highlight the need for more predictive models and mechanistic understanding. As the field progresses, aggregate science is poised to redefine the design of functional materials, shifting the focus from single molecular properties to aggregation. Advanced computational approaches including AI, machine learning, and high-throughput crystal prediction will help unravel the complex interplay among molecular interactions, packing structures, and material performance, bridging the long-standing structure–property gap in the aggregate state. Simultaneously, stimuli-responsive aggregate systems capable of dynamic excited-state modulation will emerge, enabling real-time control *via* light, heat, or electric/magnetic fields. Multicomponent strategies such as cocrystallization, doping, and supramolecular assembly will further facilitate the integration of diverse functions ranging from luminescence and thermal conversion to energy transport, opening new avenues in phototherapy, bioimaging, and flexible electronics. As our understanding deepens, molecular crystals will no longer be seen as passive molecular arrangements, but as active platforms for emergent properties, novel mechanisms, and next-generation applications. Aggregation, in this sense, marks the beginning of aggregate state material innovation.

Author contributions

Yu Zhang contributed to the conceptualization of this review, performed an extensive literature survey, prepared the figures, and wrote the original draft. Bing Bai assisted with literature organization, figure preparation, and manuscript editing. Gian Albert Alfani participated in the conceptual discussion and contributed to reviewing and editing the manuscript. Zheng Zhao and Ben Zhong Tang supervised the work, provided strategic guidance, and revised the manuscript. Yu Zhang is the first author. Zheng Zhao and Ben Zhong Tang are the corresponding authors.

Conflicts of interest

There are no conflicts to declare.

Data availability

Data availability does not apply to this article as no new data were created or analysed in this study.

Acknowledgements

This work was supported by the National Key Research and Development Program of China (2023YFB3810001), NSFC (52333007 and 52273197), Shenzhen Key Laboratory of Functional Aggregate Materials (ZDSYS20211021111400001), the Science Technology Innovation Commission of Shenzhen Municipality (KQTD20210811090142053, JCYJ20220818103007014, GJHZ20210705141810031, JCYJ20213241346130 38) and Guangdong Basic Research Center of Excellence for Aggregate Science.

Notes and references

1 B. Z. Tang, *Aggregate*, 2020, **1**, 4–5.
2 W. He, R. T. K. Kwok, Z. Qiu, Z. Zhao and B. Z. Tang, *J. Am. Chem. Soc.*, 2024, **146**, 5030–5044.
3 R. F. Chen and J. R. Knutson, *Anal. Biochem.*, 1988, **172**, 61–77.
4 G. S. Beddard and G. Porter, *Nature*, 1976, **260**, 366–367.
5 A. Mishra and P. Bäuerle, *Angew. Chem., Int. Ed.*, 2012, **51**, 2020–2067.
6 H. S. Kim, S.-R. Park and M. C. Suh, *J. Phys. Chem. C*, 2017, **121**, 13986–13997.
7 S.-J. Wu, X.-F. Fu, D.-H. Zhang, Y.-F. Sun, X. Lu, F.-L. Lin, L. Meng, X.-L. Chen and C.-Z. Lu, *Adv. Mater.*, 2024, **36**, 2401724.
8 Y. Zhang, J. Wei, D. Zhang, C. Yin, G. Li, Z. Liu, X. Jia, J. Qiao and L. Duan, *Angew. Chem., Int. Ed.*, 2022, **61**, e202113206.
9 D. Ding, K. Li, B. Liu and B. Z. Tang, *Acc. Chem. Res.*, 2013, **46**, 2441–2453.
10 H. Wang, E. Zhao, J. W. Y. Lam and B. Z. Tang, *Mater. Today*, 2015, **18**, 365–377.
11 J. Luo, Z. Xie, J. W. Y. Lam, L. Cheng, H. Chen, C. Qiu, H. Sing Kwok, X. Zhan, Y. Liu, D. Zhu and B. Zhong Tang, *Chem. Commun.*, 2001, 1740–1741.
12 N. L. C. Leung, N. Xie, W. Yuan, Y. Liu, Q. Wu, Q. Peng, Q. Miao, J. W. Y. Lam and B. Z. Tang, *Chem. – Eur. J.*, 2014, **20**, 15349–15353.
13 J. Zhang, H. Zhang, J. W. Y. Lam and B. Z. Tang, *Chem. Res. Chin. Univ.*, 2021, **37**, 1–15.
14 F. Ma, S. Zhang, J. Jiang, Y. Liu, J. Sun, J. W. Y. Lam, Z. Zhao and B. Z. Tang, *Adv. Mater.*, 2025, **37**, 2414188.
15 Y. Tu, Z. Zhao, J. W. Y. Lam and B. Z. Tang, *Matter*, 2021, **4**, 338–349.
16 Y. Zhang, S. Xie, Z. Zeng and B. Z. Tang, *Matter*, 2020, **3**, 1862–1892.
17 S. Oner and M. R. Bryce, *Mater. Chem. Front.*, 2023, **7**, 4304–4338.
18 A. A and C. A. Swamy P, *Mater. Chem. Front.*, 2025, **9**, 1794–1820.
19 E. J. Barreiro, A. E. Kümmerle and C. A. M. Fraga, *Chem. Rev.*, 2011, **111**, 5215–5246.
20 C. W. Thornber, *Chem. Soc. Rev.*, 1979, **8**, 563.
21 A. W. K. Law, T. S. Cheung, J. Zhang, N. L. C. Leung, R. T. K. Kwok, Z. Zhao, H. H. Y. Sung, I. D. Williams, Z. Qiu, P. Alam, J. W. Y. Lam and B. Z. Tang, *Adv. Mater.*, 2024, **36**, 2410739.
22 W. B. Stoll, P. A. Banks, S. G. Dannenberg, R. Waterman, L. Catalano and M. T. Ruggiero, *Cryst. Growth Des.*, 2025, **25**, 3697–3706.
23 Y. Shi, S. Wang, W. Tao, J. Guo, S. Xie, Y. Ding, G. Xu, C. Chen, X. Sun, Z. Zhang, Z. He, P. Wei and B. Z. Tang, *Nat. Commun.*, 2022, **13**, 1882.
24 N. Juneja, N. M. Shapiro, D. K. Unruh, E. Bosch, R. H. Groeneman and K. M. Hutchins, *Angew. Chem., Int. Ed.*, 2022, **61**, e202202708.
25 T. Xue, C. Ma, L. Liu, C. Xiao, S.-F. Ni and R. Zeng, *Nat. Commun.*, 2024, **15**, 1455.
26 S. Garain, S. Naz Ansari, A. Ajayan Kongasseri, B. C. Garain, S. K. Pati and S. J. George, *Chem. Sci.*, 2022, **13**, 10011–10019.
27 R. Yoshii, A. Hirose, K. Tanaka and Y. Chujo, *Chem. – Eur. J.*, 2014, **20**, 8320–8324.
28 Q. Sun, H. Wang, J. Li, F. Li, W. Zhu, X. Zhang, Q. Chen, H. Yang and W. Hu, *Small Struct.*, 2023, **4**, 2200275.
29 S.-Y. Yang, L. Zhang, F.-C. Kong, Y. Chen, W.-J. Li, F. Wang, C. Liu, X. He, X. Xiao, J. Wang, J. Sun, P. C. Y. Chow, R. T. K. Kwok, J. W. Y. Lam and B. Z. Tang, *Chem*, 2025, **11**, 102534.
30 G. Zhang, F. Chen, Y. Di, S. Yuan, Y. Zhang, X. Quan, Y. Chen, H. Chen and M. Lin, *Adv. Funct. Mater.*, 2024, **34**, 2404123.
31 L. Sun, Y. Wang, F. Yang, X. Zhang and W. Hu, *Adv. Mater.*, 2019, **31**, 1902328.
32 Z. Li, L. Liao, X. Wang, Y. Mu, Y. Huo, Z.-M. Su and F.-S. Liang, *J. Phys. Chem. Lett.*, 2023, **14**, 2187–2192.
33 Y. H. Hwang, S. Kwon, J. B. Shin, H. Kim, Y. H. Son, H. S. Lee, B. Noh, M. Nam and K. C. Choi, *Adv. Funct. Mater.*, 2021, **31**, 2009336.
34 Z. Shang, X. Yang, Q. Meng, S. Tian and Z. Zhang, *Smart Mol.*, 2023, **1**, e20220007.
35 H. Qi, W. Wu, J. Zhu, H. Zhao, H. Yu, X. Huang, T. Wang, N. Wang and H. Hao, *Chem. – Eur. J.*, 2025, **31**, e202403293.
36 L. Lan, X. Pan, P. Commins, L. Li, L. Catalano, D. Yan, H. Xiong, C. Wang, P. Naumov and H. Zhang, *CCS Chem.*, 2024, **7**, 905–917.
37 A. Luo, J. Zhang, D. Xiao, G. Xie, X. Xu, Q. Zhao, C. Sun, Y. Li, Z. Zhang, P. Li, S. Luo, X. Xie, Q. Peng, H. Li, R. Chen, Q. Chen, Y. Tao and W. Huang, *Nat. Commun.*, 2024, **15**, 8181.
38 M. Gross, F. Zhang, M. E. Arnold, P. Ravat and A. J. C. Kuehne, *Adv. Opt. Mater.*, 2024, **12**, 2301707.
39 H. Su, K. Hu, W. Huang, T. Wang, X. Zhang, B. Chen, H. Miao, X. Zhang and G. Zhang, *Angew. Chem., Int. Ed.*, 2023, **62**, e202218712.
40 Z. Yang, C. Xu, W. Li, Z. Mao, X. Ge, Q. Huang, H. Deng, J. Zhao, F. L. Gu, Y. Zhang and Z. Chi, *Angew. Chem., Int. Ed.*, 2020, **59**, 17451–17455.

41 Y. Li, S. Liu, H. Ni, H. Zhang, H. Zhang, C. Chuah, C. Ma, K. S. Wong, J. W. Y. Lam, R. T. K. Kwok, J. Qian, X. Lu and B. Z. Tang, *Angew. Chem.*, 2020, **132**, 12922–12926.
42 K. Zhou, S. Wang, L. Xu, H. Li, Y. Wang, Z. Qiu, G. Zhang, Z. Zhao and B. Z. Tang, *Matter*, 2023, **6**, 3449–3462.
43 D. Wang, M. M. S. Lee, W. Xu, G. Shan, X. Zheng, R. T. K. Kwok, J. W. Y. Lam, X. Hu and B. Z. Tang, *Angew. Chem.*, 2019, **131**, 5684–5688.
44 D. Wang, X. Kan, C. Wu, Y. Gong, G. Guo, T. Liang, L. Wang, Z. Li and Y. Zhao, *Chem. Commun.*, 2020, **56**, 5223–5226.
45 T. Li, J.-C. Liu, E.-P. Liu, B.-T. Liu, J.-Y. Wang, P.-Y. Liao, J.-H. Jia, Y. Feng and M.-L. Tong, *Chem. Sci.*, 2024, **15**, 1692–1699.
46 R. Yoshii, A. Hirose, K. Tanaka and Y. Chujo, *J. Am. Chem. Soc.*, 2014, **136**, 18131–18139.
47 X. Cao and Y. Han, *Aggregate*, 2024, **5**, e501.
48 Z. Deng, F.-C. Kong, Z. Deng, J. Zhou, S. Yang, S. He, J. Zhang, Y. Zuo, J. Wang, X. Chen, R. T. K. Kwok, G. Jia, P. C. Y. Chow, D. L. Phillips, P. Alam, J. W. Y. Lam and B. Zhong Tang, *Angew. Chem., Int. Ed.*, 2024, **63**, e202412182.
49 J. He, T. Chen, B. Yu, H. Zhang, Z. Jia, Q. Lin and S. Gong, *Sci. China Mater.*, 2025, **68**, 1057–1067.
50 J. Xu, J. Xue, Y. Dai, J. Zhang, J. Ren, C. Yao, S. Li, Q. Meng, X. Wen, H. Shao and J. Qiao, *Aggregate*, 2024, **5**, e634.
51 C. Xing, Z. Qi, Y.-J. Ma, D. Yan and W.-H. Fang, *Angew. Chem., Int. Ed.*, 2025, **64**, e202502782.
52 Z. Shuai, Q. Sun, J. Ren, T. Jiang and W. Li, *Aggregate*, 2025, **6**, e70013.
53 L. Tu, Y. Fan, C. Bi, L. Xiao, Y. Li, A. Li, W. Che, Y. Xie, Y. Zhang, S. Xu, W. Xu, Q. Li and Z. Li, *Sci. China: Chem.*, 2023, **66**, 816–825.
54 Q. Peng and Z. Shuai, *Aggregate*, 2021, **2**, e91.
55 B. M. T. C. Peluzo, R. Meena, L. Catalano, G. Schweicher and M. T. Ruggiero, *Angew. Chem.*, 2025, **137**, e202507566.
56 G. He, L. Du, Y. Gong, Y. Liu, C. Yu, C. Wei and W. Z. Yuan, *ACS Omega*, 2019, **4**, 344–351.
57 H. Wang, Q. Li, J. Zhang, H. Zhang, Y. Shu, Z. Zhao, W. Jiang, L. Du, D. L. Phillips, J. W. Y. Lam, H. H. Y. Sung, I. D. Williams, R. Lu and B. Z. Tang, *J. Am. Chem. Soc.*, 2021, **143**, 9468–9477.
58 X. He, H. Gan, J. Wu, J. Yang, Q. Jiang, J. Zhang, X. Qiao and Y. Ma, *CCS Chem.*, 2025, 1–12.
59 S. Cai, X. Yao, H. Ma, H. Shi and Z. An, *Aggregate*, 2023, **4**, e320.
60 Z. Xiong, J. Zhang, L. Wang, Y. Xie, Y. Wang, Z. Zhao, H. Zhang, S. J. Zhi, F. Huang and B. Z. Tang, *CCS Chem.*, 2023, **5**, 2832–2844.
61 J. Zhang, H. Shen, Z. Xiong, L. Du, M. Li, X. Ou, X. Zhu, J. W. Y. Lam, T.-M. Liu, C. Xu, H. Zhang and B. Zhong Tang, *Angew. Chem., Int. Ed.*, 2025, **64**, e202413751.
62 J. Zhang, L. Hu, K. Zhang, J. Liu, X. Li, H. Wang, Z. Wang, H. H. Y. Sung, I. D. Williams, Z. Zeng, J. W. Y. Lam, H. Zhang and B. Z. Tang, *J. Am. Chem. Soc.*, 2021, **143**, 9565–9574.
63 M. Lian, Y. Mu, Z. Ye, Z. Lu, J. Xiao, J. Zhang, S. Ji, H. Zhang, Y. Huo and B. Z. Tang, *Aggregate*, 2024, **5**, e560.
64 S. Ma, Y. Liu, J. Zhang, B. Xu and W. Tian, *J. Phys. Chem. Lett.*, 2020, **11**, 10504–10510.
65 H. Zhang and B. Z. Tang, *JACS Au*, 2021, **1**, 1805–1814.
66 L.-L. Yang, H. Wang, J. Zhang, B. Wu, Q. Li, J.-Y. Chen, A.-L. Tang, J. W. Y. Lam, Z. Zhao, S. Yang and B. Z. Tang, *Nat. Commun.*, 2024, **15**, 999.
67 Z. Xiong, J. Zhang, L. Wang, X. Liu, J. Z. Sun, H. Zhang and B. Z. Tang, *Chem*, 2025, **11**, 102299.
68 Y. Qi and S. Zhang, *Smart Mol.*, 2023, **1**, e20230018.
69 Z. An, C. Zheng, Y. Tao, R. Chen, H. Shi, T. Chen, Z. Wang, H. Li, R. Deng and X. Liu, *Nat. Mater.*, 2015, **14**, 685–690.
70 Y. Lu, H. Wang, Q. Li, Q. Liu, X. Zhang, Y. Jia, X. Cai, Z. Zhao, Y. Huan and B. Z. Tang, *Smart Mol.*, 2025, **3**, e20240011.
71 W. Zhao, Z. He, J. W. Y. Lam, Q. Peng, H. Ma, Z. Shuai, G. Bai, J. Hao and B. Z. Tang, *Chem*, 2016, **1**, 592–602.
72 W. Zhao, Z. He and B. Z. Tang, *Nat. Rev. Mater.*, 2020, **5**, 869–885.
73 Z. Yang, Z. Mao, X. Zhang, D. Ou, Y. Mu, Y. Zhang, C. Zhao, S. Liu, Z. Chi, J. Xu, Y.-C. Wu, P.-Y. Lu, A. Lien and M. R. Bryce, *Angew. Chem.*, 2016, **128**, 2221–2225.
74 W. Zhao, T. S. Cheung, N. Jiang, W. Huang, J. W. Y. Lam, X. Zhang, Z. He and B. Z. Tang, *Nat. Commun.*, 2019, **10**, 1595.
75 Z. Xiong, J. Zhang, J. Z. Sun, H. Zhang and B. Z. Tang, *J. Am. Chem. Soc.*, 2023, **145**, 21104–21113.
76 J. Zhang, P. Alam, S. Zhang, H. Shen, L. Hu, H. H. Y. Sung, I. D. Williams, J. Sun, J. W. Y. Lam, H. Zhang and B. Z. Tang, *Nat. Commun.*, 2022, **13**, 3492.
77 F. Ma, B. Wu, S. Zhang, J. Jiang, J. Shi, Z. Ding, Y. Zhang, H. Tan, P. Alam, J. W. Y. Lam, Y. Xiong, Z. Li, B. Z. Tang and Z. Zhao, *J. Am. Chem. Soc.*, 2025, **147**, 10803–10814.
78 B. Zhang, B. Li, H. Zhang, B. Ma, J. Lou, X. Dong, D. Yang, B. Z. Tang and Z. Wang, *Aggregate*, 2025, **6**, e726.
79 K. Uemura, K. Tanaka and Y. Chujo, *Crystals*, 2022, **12**, 688.
80 C. Tang, L. Song, K. Zhou, P. Ren, E. Zhao and Z. He, *Chem. Sci.*, 2023, **14**, 1871–1877.
81 M. Chen, G. Hu, Z. Xiong, H. Hu, J. Z. Sun, H. Zhang and B. Z. Tang, *Polym. Chem.*, 2025, **16**, 1120–1125.
82 L. Euringer, M. Holzapfel, I. Krummenacher, M. Franz, S. Richert, H. Braunschweig and C. Lambert, *J. Am. Chem. Soc.*, 2024, **146**, 27679–27689.
83 W. Lai, Y. Bu, W. Xiao, H. Liu, J. Guo, L. Zhao, K. Yang, S. Xie and Z. Zeng, *J. Am. Chem. Soc.*, 2023, **145**, 24328–24337.
84 I. C.-Y. Hou, L. Li, H. Zhang and P. Naumov, *Smart Mol.*, 2024, **2**, e20230031.
85 Z. Zhou, K. Yang, L. He, W. Wang, W. Lai, Y. Yang, Y. Dong, S. Xie, L. Yuan and Z. Zeng, *J. Am. Chem. Soc.*, 2024, **146**, 6763–6772.
86 X. Zhao, J. Gong, P. Alam, C. Ma, Y. Wang, J. Guo, Z. Zeng, Z. He, H. H. Y. Sung, I. D. Williams, K. S. Wong, S. Chen, J. W. Y. Lam, Z. Zhao and B. Z. Tang, *CCS Chem.*, 2021, **4**, 1912–1920.
87 K. J. Meers, T. N. Tran, Q. Zheng, D. K. Unruh and K. M. Hutchins, *Cryst. Growth Des.*, 2020, **20**, 5048–5060.

88 M. Liu, H. Tan, B. B. Chen, C. Lu, B. Wu, Y. Zhu, R. Zhang, Z. Tian, Y. Luo, Z. Zhao and B. Z. Tang, *ACS Nano*, 2025, **19**, 21068–21082.
89 W. Chen, S. Sun, G. Huang, S. Ni, L. Xu, L. Dang, D. L. Phillips and M.-D. Li, *J. Phys. Chem. Lett.*, 2021, **12**, 5796–5801.
90 S. Liu, Y. Pei, Y. Sun, Z. Wang, H. Chen, D. Zhu, M. R. Bryce, B. Z. Tang and Y. Chang, *Aggregate*, 2024, **5**, e547.
91 W. Ma, Y. Su, Q. Zhang, C. Deng, L. Pasquali, W. Zhu, Y. Tian, P. Ran, Z. Chen, G. Yang, G. Liang, T. Liu, H. Zhu, P. Huang, H. Zhong, K. Wang, S. Peng, J. Xia, H. Liu, X. Liu and Y. M. Yang, *Nat. Mater.*, 2022, **21**, 210–216.
92 M. Chen, L. Sun, X. Ou, H. Yang, X. Liu, H. Dong, W. Hu and X. Duan, *Adv. Mater.*, 2021, **33**, 2104749.
93 N. Gan, X. Zou, M. Dong, Y. Wang, X. Wang, A. Lv, Z. Song, Y. Zhang, W. Gong, Z. Zhao, Z. Wang, Z. Zhou, H. Ma, X. Liu, Q. Chen, H. Shi, H. Yang, L. Gu, Z. An and W. Huang, *Nat. Commun.*, 2022, **13**, 3995.
94 L. Lu, M. Sun, Q. Lu, T. Wu and B. Huang, *Nano Energy*, 2021, **79**, 105437.
95 Q.-S. Zhang, X.-D. Zhang, J.-Y. Zhuang and M. Pan, *Aggregate*, 2024, **5**, e456.
96 M. Nikl, A. Yoshikawa, K. Kamada, K. Nejezchleb, C. R. Stanek, J. A. Mares and K. Blazek, *Prog. Cryst. Growth Charact. Mater.*, 2013, **59**, 47–72.
97 V. V. Nagarkar, T. K. Gupta, S. R. Miller, Y. Klugerman, M. R. Squillante and G. Entine, *IEEE Trans. Nucl. Sci.*, 1998, **45**, 492–496.
98 X. Chen, Z.-C. Zhang, K. Zhang, X.-Y. Guan, X.-F. Weng and H.-T. Han, *IEEE Trans. Nucl. Sci.*, 2020, **67**, 1893–1898.
99 M. Dong, Z. Wang, Z. Lin, Y. Zhang, Z. Chen, Y. Wu, H. Ma, Z. An, L. Gu and W. Huang, *J. Am. Chem. Soc.*, 2025, **147**, 4069–4078.
100 X. Wang, W. Sun, H. Shi, H. Ma, G. Niu, Y. Li, J. Zhi, X. Yao, Z. Song, L. Chen, S. Li, G. Yang, Z. Zhou, Y. He, S. Qu, M. Wu, Z. Zhao, C. Yin, C. Lin, J. Gao, Q. Li, X. Zhen, L. Li, X. Chen, X. Liu, Z. An, H. Chen and W. Huang, *Nat. Commun.*, 2022, **13**, 5091.
101 Y.-H. Chen, G.-Z. Zhang, F.-H. Chen, S.-Q. Zhang, X. Fang, H.-M. Chen and M.-J. Lin, *Chem. Sci.*, 2024, **15**, 7659–7666.
102 R.-Y. Cao, Y.-B. Si, Q. Yang, Z.-Y. Gao, J.-W. Yuan, Y. Zhao, Q.-C. Peng, K. Li, S.-Q. Zang and B. Z. Tang, *Natl. Sci. Rev.*, 2025, **12**, nwaf045.
103 X. Yu, H. Zhang and J. Yu, *Aggregate*, 2021, **2**, 20–34.
104 F. Ma, Z. Gao, Q. Jia, Y. Yang, B. Wang, J. Zhang, Z. Deng, R. Mo, Z. Ding, G. Xing, Y. Liu, Z. Wang, K. Wang, J. W. Y. Lam, D. Ding, Z. Zhao and B. Z. Tang, *ACS Nano*, 2025, **19**, 1676–1688.
105 J. Gu, W. Yuan, K. Chang, C. Zhong, Y. Yuan, J. Li, Y. Zhang, T. Deng, Y. Fan, L. Yuan, S. Liu, Y. Xu, S. Ling, C. Li, Z. Zhao, Q. Li, Z. Li and B. Z. Tang, *Angew. Chem.*, 2025, **137**, e202415637.
106 J. Qi, W. Qiao and Z. Y. Wang, *Chem. Rec.*, 2016, **16**, 1531–1548.
107 J. Deng, Z. Zhang, P. Sang, S. Yin, S. Zhang, Y. Li, B. Yang, C. Gu and Y. Ma, *Aggregate*, 2023, **4**, e313.
108 E. Thimsen, B. Sadtler and M. Y. Berezin, *Nanophotonics*, 2017, **6**, 1043–1054.
109 W.-Z. Sun, W.-J. Zhang, J.-T. Xu, D.-Q. Liu, B.-Q. Ou, L. Chen, J.-W. Ye and X.-M. Chen, *Aggregate*, 2025, **6**, e721.
110 Y. Wang, H. Wu, P. Li, S. Chen, L. O. Jones, M. A. Mosquera, L. Zhang, K. Cai, H. Chen, X.-Y. Chen, C. L. Stern, M. R. Wasielewski, M. A. Ratner, G. C. Schatz and J. F. Stoddart, *Nat. Commun.*, 2020, **11**, 4633.
111 M.-P. Zhuo, Y. Yuan, Y. Su, S. Chen, Y.-T. Chen, Z.-Q. Feng, Y.-K. Qu, M.-D. Li, Y. Li, B.-W. Hu, X.-D. Wang and L.-S. Liao, *Adv. Mater.*, 2022, **34**, 2107169.
112 Y. D. Zhao, W. Jiang, S. Zhuo, B. Wu, P. Luo, W. Chen, M. Zheng, J. Hu, K.-Q. Zhang, Z.-S. Wang, L.-S. Liao and M.-P. Zhuo, *Sci. Adv.*, 2023, **9**, eadh8917.
113 S. Yang, Q. Jia, X. Ou, F. Sun, C. Song, T. Zhao, R. T. K. Kwok, J. Sun, Z. Zhao, J. W. Y. Lam, Z. Wang and B. Z. Tang, *J. Am. Chem. Soc.*, 2025, **147**, 3570–3583.
114 S. Xue, Z. Shi, Z. Wang, H. Tan, F. Gao, Z. Zhang, Z. Ye, S. Nian, T. Han, J. Zhang, Z. Zhao, B. Z. Tang and Q. Zhang, *Nat. Commun.*, 2024, **15**, 10084.
115 L. Jiang, S. Zhou, J. Yang, H. Wang, H. Yu, H. Chen, Y. Zhao, X. Yuan, W. Chu and H. Li, *Adv. Funct. Mater.*, 2022, **32**, 2108977.
116 Q. Shen, L. Wang, X. Ruan, N. Li, W. Wang, W. Wang, J. Shao and X. Dong, *Adv. Funct. Mater.*, 2023, **33**, 2300023.
117 B. Liu and B. Z. Tang, *Angew. Chem., Int. Ed.*, 2020, **59**, 9788–9789.
118 Y. Gong, Y. Tan, H. Li, Y. Zhang, W. Yuan, Y. Zhang, J. Sun and B. Z. Tang, *Sci. China: Chem.*, 2013, **56**, 1183–1186.
119 K. Gu, Z. Meng, X. W. Liu, Y. Wu, X. Qi, Y. Ren, Z.-Q. Yu and B. Z. Tang, *Aggregate*, 2023, **4**, e337.
120 A. V. Kumar, M. Godumala, J. Ravi and R. Chandrasekar, *Angew. Chem., Int. Ed.*, 2022, **61**, e202212382.
121 S. Chen, M.-P. Zhuo, X.-D. Wang, G.-Q. Wei and L.-S. Liao, *PhotoniX*, 2021, **2**, 2.
122 Z. Qi, Y.-J. Ma and D. Yan, *Aggregate*, 2024, **5**, e411.
123 S. Du, S. Ma, B. Xu and W. Tian, *J. Phys. Chem. Lett.*, 2021, **12**, 9233–9238.
124 M. Rohullah, V. V. Pradeep, S. Singh and R. Chandrasekar, *Nat. Commun.*, 2024, **15**, 4040.

